

**Evaluation of correlated Pandora column NO₂ and *in situ* surface NO₂
measurements during GMAP campaign**

Lim-Seok Chang¹, Donghee Kim¹, Hyunkee Hong¹, Deok-Rae Kim¹, Jeonga Yu¹,
Kwangyul Lee¹, Hanlim Lee², Daewon Kim², Jinkyu Hong³, Hyun-Young Jo⁴,
and Cheol-Hee Kim^{4, 5}

¹ *Environmental Satellite Center, National Institute of Environmental Research, Incheon, 22689, Republic of Korea*

² *Department of Spatial Information Engineering, Pukyong National University, Busan, 48547, Republic of Korea*

³ *Department of Atmospheric Sciences, Yonsei University, Seoul, 03722, Republic of Korea*

⁴ *Institute of Environmental Studies, Pusan National University, Busan, 46241, Republic of Korea*

⁵ *Department of Atmospheric Sciences, Pusan National University, Busan, 46241, Republic of Korea*

Correspondence:

Cheol-Hee Kim (chkim2@pusan.ac.kr), and Lim-Seok Chang (lschang@korea.kr)

1 **Abstract.**

2 To validate the Geostationary Environment Monitoring Spectrometer (GEMS), the GEMS
3 Map of Air Pollution (GMAP) campaign was conducted during 2020–2021 by integrating
4 Pandora Asia Network, aircraft, and *in situ* measurements. In the present study, GMAP-2020
5 measurements were applied to evaluate urban air quality and explore the synergy of Pandora
6 column (PC) NO₂ measurements and surface *in situ* (SI) NO₂ measurements for Seosan, South
7 Korea, where large point source (LPS) emissions are densely clustered. Due to the difficulty
8 of interpreting the effects of LPS emissions on air quality downwind of Seosan using SI
9 monitoring networks alone, we explored the combined analysis of both PC-NO₂ and SI-NO₂
10 measurements. Agglomerative hierarchical clustering using vertical meteorological variables
11 combined with PC-NO₂ and SI-NO₂ yielded three distinct conditions: synoptic wind-dominant
12 (SD), mixed (MD), and local wind-dominant (LD). These results suggest meteorology-
13 dependent correlations between PC-NO₂ and SI-NO₂. Overall, yearly daytime mean (11:00–
14 17:00 KST) PC-NO₂ and SI-NO₂ statistical data showed good linear correlations ($R = \sim 0.73$);
15 however, the differences in correlations were largely attributed to meteorological conditions.
16 SD conditions characterized by higher wind speeds and advected marine boundary layer
17 heights suppressed fluctuations in both PC-NO₂ and SI-NO₂, driving a uniform vertical NO₂
18 structure with higher correlations, whereas under LD conditions, LPS plumes were decoupled
19 from the surface or were transported from nearby cities, weakening correlations through
20 anomalous vertical NO₂ gradients. The discrepancies suggest that using either PC-NO₂ or SI-
21 NO₂ observations alone involves a higher possibility of uncertainty under LD conditions or
22 prevailing transport processes. However, under MD conditions, both pollution ventilation due
23 to high surface wind speeds and daytime photochemical NO₂ loss contributed to stronger
24 correlations through a decline in both PC-NO₂ and SI-NO₂ toward noon. Thus, Pandora Asia
25 Network observations collected over 13 Asian countries since 2021 can be utilized for detailed
26 investigation of the vertical complexity of air quality, and the conclusions can be also applied
27 when performing GEMS observation interpretation in combination with SI measurements.

28

29 **1. Introduction**

30 Rapid developments in environmental remote sensing have led to a new era of air quality
31 observations, and recent hyperspectral data retrieval technologies have allowed for routine and

32 accurate monitoring of air pollutants at high spatial and temporal resolution. In particular, the
33 Geostationary Environment Monitoring Spectrometer (GEMS), which was launched on
34 February 18, 2020, measures the total and tropospheric air pollutant columns hourly at spatial
35 resolutions of $7 \text{ km} \times 8 \text{ km}$ for gas and $3.5 \text{ km} \times 8 \text{ km}$ for aerosols (Kim et al., 2020), facilitating
36 the tracking of pollution transport from local to synoptic scales.

37 Recent studies have revealed the potential of satellite observations to evaluate surface air
38 quality, particularly in regions with sparse air quality-monitoring networks. The main approach
39 is to convert column density to surface concentrations using a shape factor of the ratio of the
40 partial column (Ω_{z_0}) within the lowest layer (z_0) to the total column (Ω_{total}) (Zhao *et al.*, 2019),
41 as follows:

$$42 \quad S = \frac{\Omega_{z_0}}{\Omega_{\text{total}}} \times \frac{C}{\Delta z_0} ,$$

43 where S , C , and Δz_0 are the surface concentration, column density, and lowest layer thickness,
44 respectively. Acquiring accurate profile shape information is critical for determining the
45 relationship between the column amount and surface concentration because the shape factor is
46 spatiotemporally variable. Considering this, numerous studies have obtained close
47 relationships using chemical transport model simulations, aircraft *in situ* measurements, and
48 satellite observations with high correlation coefficients (R) of 0.7 or more and used them to
49 scale up surface NO_2 to column NO_2 (Wang and Christopher, 2003; Boersma *et al.*, 2009;
50 Lamsal *et al.*, 2010). This strong correlation can be explained by the generally uniform
51 planetary boundary layer height (PBLH), and by aerosol type and abundance, which is also the
52 case for trace gases.

53 By contrast, the implications of weak correlations between column and surface
54 measurements remain unclear. Engel-Cox *et al.* (2004) found a negative correlation of AOD
55 and surface $\text{PM}_{2.5}$ in northwestern USA, and explained it based on elevated haze decoupled

56 from the surface. Thompson *et al.* (2019) examined weak correlations between Pandora column
57 (PC) measurements and surface *in situ* (SI) observations of NO₂ over the Yellow Sea during
58 the Korea–US air quality (KORUS-AQ) field study, and suggested, as a possible reason, the
59 transported non-uniform plumes originated in China and Seoul hundreds of meters above the
60 ground from the surface layer. The estimated surface PM_{2.5} concentration was weakly
61 correlated ($R = 0.4\text{--}0.49$) with observed PM_{2.5} concentrations in Seoul, because only PBLH
62 was added to the multi-linear regression model to correlate AOD to surface PM_{2.5} (Kim *et al.*,
63 2021). This effect may be related to the significant impact of long-range transport on PM_{2.5},
64 with a contribution of up to 39% in Seoul (Lee *et al.*, 2021). Thus, the wide variability in the
65 degree of correlation between PC-PM and SI-PM is closely related to vertical profile variability
66 (Flynn *et al.*, 2016).

67 It appears highly probable that several factors are responsible for the correlations between
68 PC-NO₂ and SI-NO₂; therefore, it is necessary to improve our understanding of the degree of
69 correlation through detailed measurements, including column concentration. In this study, we
70 focused on the impact of meteorology and chemistry on correlation variability using PC, SI
71 and aircraft measurements, as well as meteorological observations. Understanding vertical
72 profile variability is also useful for evaluating the effects of various emissions on urban air
73 quality, particularly in areas neighboring active large point source (LPS) emissions sites.
74 Quantifying the impact of LPS emissions on downwind cities remains challenging due to the
75 lack of three-dimensional (3D) measurements. Accurate vertical profile data are also useful for
76 improving remote sensing retrieval algorithms, because the profile shape contributes to the
77 conversion of slant column density into vertical column density as part of the air mass factor.
78 In mid-2019, the Pandonia Global Network (PGN; <https://pandonia-global-network.org>) was
79 launched, with support from the National Aeronautics and Space Administration (NASA) and
80 European Space Agency (ESA), to facilitate the validation and verification of low-orbit or

81 geostationary environmental satellites. This network is attempting to expand air quality
82 monitoring through integration with existing long-term air quality monitoring stations. Since
83 2020, the National Institute of Environmental Research, Economic and Social Commission for
84 Asia and the Pacific, and Korea Environment Corporation have been extending the Pandora
85 Asia Network to include 13 Asian countries, with support from the Korea International
86 Cooperation Agency. The Pandora Asia Network is expected to be widely used to study urban
87 air quality in Asia, which is increasingly deteriorating due to rapid economic growth.

88 As part of the GEMS Map of Air Pollution (GMAP) campaign, a suite of Pandora
89 instruments was deployed in Seosan, a South Korean coastal city, from November 2020 to
90 January 2021 (GMAP-2020), and we applied GMAP-2020 measurements to explore the
91 synergy of PC observations when evaluating air quality over Seosan. Further results from this
92 research project are also reported in this special issue, including GEMS validation and urban
93 air quality evaluations based on Pandora, aircraft, surface flux, and *in situ* surface chemical
94 measurements conducted during GMAP-2020.

95

96 **2. GMAP-2020 campaign**

97 GEMS was launched on February 19, 2020; it is the first instrument to observe air quality from
98 a geostationary Earth orbit. GEMS provides hourly air quality data on aerosols and gases at a
99 spatial resolution of 7 km × 8 km. It is a scanning ultraviolet (UV)-visible spectrometer that
100 observes key atmospheric constituents including O₃, NO₂, CO, SO₂, CH₂O, CHOCHO,
101 aerosols, clouds, and UV indices. This mission heralded a new era of satellite air quality
102 monitoring and will be joined by NASA's Tropospheric Emissions: Monitoring of Pollution
103 (TEMPO) and ESA's Sentinel-4 to form the GEO Air Quality Constellation in ~3 years, to
104 cover the most polluted region in the Northern Hemisphere.

105 During GMAP-2020, Pandora instruments (PA₁–PA₄) were deployed near large point

106 sources (LPS₁–LPS₄) in Seosan; *in situ* surface air quality monitoring systems (AQM₁–AQM₆)
107 and meteorological observations (Met₁–Met₃) were also used in this study (see their locations
108 in Fig. 1). Aircraft measurements were also used to validate GEMS and diagnose LPSs located
109 in industrial areas surrounding Seosan. We explored the synergy of Pandora observations and
110 SI measurements, based on measurements collected during GMAP-2020, by evaluating air
111 quality in industrial Seosan (where LPSs are densely clustered). We particularly investigated
112 the impacts of vertical profile and sub-pixel variability for trace gases and aerosols, for further
113 GEMS validation. All measurement sites for both GMAP-2020 campaigns are indicated in
114 Figure 1.

115

116 **3. Methods**

117 **3.1 Study area**

118 Seosan, the target area of the GMAP-2020 campaign, is a small city with a population of
119 174,780 in 2017; it is accessed via three expressways to the east and four national highways
120 cross the city. It is located in midwestern South Korea, and is affected by >300 emissions point
121 sources including LPSs. Coal-fired power plants including Taean, Dangjin, the Hyundai
122 Dangjin steelworks, and the Daesan petrochemistry industrial complex (LPS₁–LPS₄,
123 respectively, in Fig. 1) have the highest emissions rates in South Korea. The Hyundai Dangjin
124 steelworks (LPS₃) and Taean and Dangjin power plants (LPS₁ and LPS₂) emit 10.5, 11, and
125 8.8 Gg of NO_x per year, respectively. Although Seosan accounts for only 1.8% of the
126 population of Seoul, its NO_x emissions (10.2 Gg year⁻¹) account for 13.2% of its total NO_x
127 emissions. The transportation sector of Seosan is a far greater NO_x source than the industrial
128 sector of Seoul (ratio of 99:1); however, within Seosan, the industrial sector is on par with the
129 transport sector (52:48; <http://airemiss.nier.go.kr>).

130 During the past decade, the annual mean NO₂ level in Seosan has been 17 ppb, which is

131 approximately half of that in Seoul (31.2 ppb). NO₂ exhibits strong seasonal variation, reaching
132 a minimum in summer and maximum in winter, due to meteorological factors and greater
133 energy use during winter (Kim and Kim, 2020). Therefore, the timing of the GMAP-2020
134 campaign was well suited to tracking pollution.

135

136 **3.2 Pandora measurements**

137 Pandora measures the UV and visible wavelengths (280–525 nm) of direct sunlight with a
138 spectral resolution of 0.6 nm, to determine the vertical column density of NO₂, O₃, and HCHO
139 (Herman *et al.*, 2009). For measurements in Dobson units (DU; 1 DU = 26.9 Pmol cm⁻²),
140 column NO₂ has a very high signal-to-noise ratio (700:1) and very high precision (0.01 DU)
141 for clear skies (Herman *et al.*, 2009). The vertical column density of NO₂ can be determined
142 using DOAS software (Van Roozendael and Fayt, 2001). Pandora direct-sun measurements are
143 advantageous in that the air mass factor is simplified, and therefore is dependent only on the
144 geography for a known solar zenith angle.

145 From retrieved Pandora measurements, tropospheric and total (=tropospheric +
146 stratospheric) vertical column densities are both available. However, it should be noted that
147 appreciable uncertainties cannot be neglected in the tropospheric NO₂ profiles obtained from
148 Pandora instruments, particularly for the high aerosol-loading areas such as East Asia. In this
149 background, we used total vertical column densities in the present study, and also confirmed
150 that they have a high correlation with the tropospheric column densities observed in our study
151 period with little change in stratospheric column density in space and time at the local scale.

152 Four Pandora instruments were installed at sites to the south of LPSs (Fig. 1) during the
153 GMAP-2020 campaign, i.e., at Seosan Daehoji, Seosan Dongmun, Seosan City Council, and
154 Seosan Super Site (PA₁–PA₄ in Fig. 1). The presence of clouds reduces vertical column density
155 precision by decreasing the number of photons arriving at Pandora instruments within a fixed

156 integration time. Therefore, the retrieved Pandora measurements were cloud-screened using an
157 observed cloud cover of 0.6. Cloud cover was provided by the Korea Meteorological
158 Administration (KMA), and the precision improvement afforded by cloud screening was
159 verified by comparing each Pandora-derived vertical column density with the median vertical
160 column density, with and without cloud screening within the inter-comparison period.

161 At PA₄, the operating period was extended to cover almost the entire year (November 12,
162 2020–October 30, 2021) including the GMAP-2020 campaign period, and the Pandora spectra
163 were processed into vertical column density data for trace gases using the standard NO₂
164 algorithm in BlickP software provided by PGN (Cede, 2019). The resultant PC-NO₂ data were
165 obtained from the PGN website (<https://pandonia-global-network.org>) for the 1-year period
166 from Nov. 12, 2020 to Oct. 30, 2021, and were also used as PC-NO₂ statistics for PA₄, in this
167 study.

168

169 **3.3 Surface and airborne chemical measurements**

170 Hourly average data for SI-NO₂ over a period of 1 year were obtained from Ministry of
171 Environment AQM network stations in Seosan: Pandori, Leewon, Taeon, Dongmoon,
172 Seongyeon, and Daesan (AQM₁–AQM₆, respectively, in Fig. 1). The Seosan Super Site
173 (PA₄/AQM₁) provided hourly data for NO and NO_y via an NO-DIF-NO_y analyzer (42i-Y;
174 Thermo Scientific, Waltham, MA, USA), and for PM_{2.5} chemical species using an ambient ion
175 monitor (AIM; URG 9000D, URG Corp., Chapel Hill, NC, USA). Weekly zero and span
176 checks were conducted for NO_y calibration, to ensure that differences between checks
177 remained <3%. Water-soluble ions in aerosol and gaseous species were measured hourly using
178 an AIM, and ion mass balance was used to ensure data quality under the quality control
179 procedures of the AQM network installation and operation guidelines (NIER, 2021).

180 Aircraft measurements were conducted during the GMAP-2020 campaign period, and

181 nine flights were conducted on 8 days (Nov. 26, 27, and 28 and Dec. 1, 6, 8, 9, and 12, 2020).
182 The horizontal and vertical distributions of NO₂ and O₃ over Seosan were measured during
183 GMAP-2020 using an NO₂ monitor (T500U; Teledyne, Thousand Oaks, CA, USA) and an O₃
184 analyzer (TEI49C; Thermo Scientific) onboard the Cessna Grand Caravan 208 B. These
185 instruments had response times of <40 and <20 s, and detection limits of 40 ppt and 1 ppb,
186 respectively. The flight paths included a raster mode over all of Seosan at a height of 500–700
187 m and a profiling mode from 500 m to 1.5 km over PA₁ and PA₄ (Fig. 2).

188

189 **3.4 Meteorological measurements**

190 Ground-based hourly observation data for meteorological variables were obtained from Seosan
191 Automated Synoptic Observing System (ASOS) stations maintained by the KMA, and wind
192 and temperature profile data were obtained twice daily (0000 and 1200 UTC) via a rawinsonde
193 instrument at the Osan World Meteorological Organization upper air measurement station
194 (47122) near Seosan. Due to time constraints of the sonde measurements, information on PBLH
195 variation was obtained from Unified Model (UM) simulation results provided on the KMA
196 website (<https://afso.kma.go.kr>).

197 During the GMAP-2020 campaign, a 3D sonic anemometer (CPEC200; Campbell
198 Scientific, Logan, UT, USA) was also installed on the rooftop at PA₄ for turbulent flux
199 measurements at the city–atmosphere interface (Hong *et al.*, 2019). All wind components and
200 sonic temperatures were measured at a 10 Hz sampling rate, and ground-level sensitive heat
201 flux was measured directly using a 30 min averaging period. Quality controls such as double
202 rotation, spike removal, and outlier filtering were also applied.

203

204 **3.5 Correlation analyses**

205 We examined the synergy of PC and SI data obtained during the GMAP-2020 campaign, and

206 combined these measurement data to evaluate air quality in Seosan, South Korea. We attempted
207 to interpret the meteorological and photochemistry data measured during GMAP-2020, and to
208 demonstrate that caution is required when attempting to study the vertical structure of air
209 pollutants using either surface observations or satellite data only, particularly in industrial
210 areas.

211 First, we examined the combined use of year-long PC-NO₂ and SI-NO₂
212 measurements, and investigated the factors modulating their correlation. Numerous studies
213 have examined the correlations between chemical species, including aerosols (Thomson et
214 al., 2019; Wang et al., 2019; Kim et al., 2012; Jo et al., 2013; Sanchez et al., 1990; Kim et al.,
215 2018). Wang *et al.* (2019) reported that aerosols moderately correlate with NO₂ due to the
216 frequent occurrence of lifted layers probably related to the transport of pollutants. Jo *et al.*
217 (2013) differentiated haze types using the trajectory speed and direction and different synoptic
218 conditions. In this background, we hypothesized that their differences in PC-NO₂ and SI-NO₂
219 were due to meteorological conditions, and performed k-means and agglomerative hierarchical
220 cluster analyses of various meteorological variables. Clustering is the grouping of objects that
221 are alike and are different from the objects belonging to other clusters. As a first step, k-means
222 Clustering was applied to find smaller clusters until each object was classified in one cluster.
223 Subsequently, agglomerative hierarchical steps are applied to make up for the shortcomings of
224 k-means clustering, in which once merging (or splitting) is done, it can never be undone. More
225 details are found in Venkat Reddy *et al.* (2017). We used XLSTAT software (Addinsoft, Paris,
226 France) for the cluster analysis with eight meteorological variables representing local and
227 synoptic circulations in the cluster analysis: surface wind speed (W_{sfc}), 925 hPa temperature
228 (T₉₂₅), sea level pressure (P_{sfc}), pressure tendency (dP_{sfc}/dt), 850 hPa wind speed (W₈₅₀)
229 and its north–south and east–west components (NS₈₅₀ and EW₈₅₀), and 500 hPa geopotential
230 height (GPH₅₀₀). We subtracted 30-day moving averages from all data to account for typical

231 seasonal variation. Monthly averages were used for PC-NO₂ analysis due to the limited
232 availability of hourly data.

233 Correlations between PC-NO₂ and SI-NO₂ were analyzed in each meteorological group
234 and the impact of photochemistry was interpreted based on case-specific features. We also
235 investigated correlations in association with near-surface micrometeorological variables such
236 as PBLH in each meteorological group.

237

238 **4. Results and Discussion**

239

240 **4.1 Correlation analysis results for PC-NO₂ and SI-NO₂**

241 The yearly PC-NO₂ statistics at four Pandora sites (PA₁–PA₄) are summarized in Table 1. The
242 total averaged PC-NO₂ over all sites was 0.45 DU during GMAP-2020, which is well above
243 the typical values (0.1–0.2 DU) for Anmyeondo (the location is shown in Figure 1), a
244 representative background site (Herman *et al.*, 2018). Although site PA₃ is located in a rural
245 area, it nevertheless exhibited the highest PC-NO₂ amounts, suggesting that plumes were
246 frequently transported from nearby point sources and/or urban areas.

247 Scatter diagrams of hourly PC-NO₂ and SI-NO₂ measurements from Pandora sites PA₁–
248 PA₃ (GMAP-2020) and PA₄ (yearly measurement; November 12, 2020–October 30, 2021) are
249 shown in Fig. 3a. These hourly data had a fair 1:1 linear relationship ($R = 0.41$), implying the
250 overall uniformity of NO₂ profiles, whereas the linear relationship with PC-NO₂ weakened as
251 SI-NO₂ levels increased (Fig. 3a). It appears that the SI-NO₂ has a distinct diurnal change
252 despite the same PC-NO₂, and higher variable surface NO₂ levels may result from the relatively
253 weaker linear relationship between PC-NO₂ and SI-NO₂. To explore these anti-correlation
254 cases further, we selected the lower and upper bounds of the tendencies; these are plotted in
255 Fig. 3b, which shows that PC-NO₂ was positively correlated with SI-NO₂ on February 24, 2021

256 ($R = 0.88$), while a negative correlation occurred on April 21, 2021 ($R = -0.88$), indicating a
257 wide range of case-specific correlations. The negative correlation on April 21 (Fig. 3b) implied
258 that the nonhomogeneous NO_2 distributions vertically were partially due to the photochemical
259 process. For example, the decrease in PC- NO_2 despite an increase in SI- NO_2 might have
260 occurred because NO_2 is removed by photochemical loss; it can occur more severely in the
261 upper atmosphere with high OH concentrations. Another possible reason is the occurrence of
262 lifted layers related to pollutant transport, yielding sharp changes in vertical concentration from
263 the surface to the upper layer. The case-specific discussion follows.

264

265 **4.2 Impacts of meteorological conditions on correlations between PC- NO_2 and SI- NO_2**

266 Our k-means cluster analysis distinguished three groups with the lowest within-group variance
267 and largest among-group variance. Among the total of 141 cases, 47, 66, and 28 were classified
268 into groups 1–3, respectively. Thus, group 2 had the largest proportion of cases (47%) and
269 group 3 had the smallest (20%). The combination of meteorological components in group 1
270 indicated the end of a high-pressure system ($P_{\text{sfc}} > 0$, $dP_{\text{sfc}}/dt < 0$), with southerly winds
271 ($NS850 > 0$) bringing warmer air ($T925 > 0$) to the region, leading to stable atmospheric
272 stratification and weak surface winds (Fig. 4). This group 1 meteorological mode appeared to
273 result in very weak NO_2 ventilation, which produced the highest PC- NO_2 and SI- NO_2 values.
274 Group 3 showed the opposite trend, with strong northerly winds bringing colder air into the
275 region, leading to an unstable atmosphere and stronger surface winds, and ultimately
276 decreasing PC- NO_2 and SI- NO_2 to their lowest levels.

277 SI- NO_2 was approximately twice as high in group 1 than group 3, whereas PC- NO_2
278 showed no significant difference (Fig. 4a). We hypothesized that PBLH might also differ
279 significantly under these micrometeorological conditions; therefore, we further explored daily
280 maximum PBLH simulated by the Global Forecast System (GFS) and Lagrangian backward

281 trajectories obtained from Hybrid Single-Particle Lagrangian Integrated Trajectory
 282 (HYSPLIT) and GFS system for the 141 cases. The mean simulated PBLH in Seosan, our study
 283 area, was 942.1 ± 405.3 m for 2020, which was similar to the annual mean daily maximum
 284 PBLH (1,013.6 m) in Osan (Lee *et al.*, 2013). However, the simulated PBLH differed
 285 significantly among the three groups (767.0 ± 304.8 , 923.2 ± 335.3 , and $1,280.6 \pm 501.2$ m for
 286 groups 1–3, respectively). The PBLH for group 3 was 1.7-fold higher than that for group 1
 287 (Fig. 4k). We also detected significant differences among the three groups in synoptic
 288 components of the lower troposphere including W850, as well as in local meteorological
 289 parameters such as the sea breeze index (SBI) suggested by Biggs and Graves (1962), which
 290 is defined as, $SBI = \frac{U^2}{C_p \Delta T}$, where U is Wsfc (Fig. 4c), C_p is specific heat, and ΔT is the
 291 temperature difference between T925 and the sea surface temperature. Thus, the SBI represents
 292 the ratio between inertial ($\rho U^2/2$) and buoyance forces ($\rho g C_p \Delta T$), where ρ is air density and g
 293 is gravity, and its value provides an indication of the likelihood of local circulation events such
 294 as sea breezes; at higher SBIs (i.e., $SBI > 3$), sea breezes cannot overcome the prevailing wind,
 295 whereas lower SBIs (i.e., $0 < SBI < 3$) can indicate strong sea breezes.

296 In the example shown in Fig. 4l, the SBI for groups 1–3 was 0.1 ± 4.5 , 0.1 ± 9.2 , and -0.2
 297 ± 12.5 , respectively. Most SBIs in group 1 ranged from 0 to 3, indicating that group 1
 298 corresponded to the dominant local circulation (LD), whereas the SBIs in group 3 had the
 299 lowest frequencies comparing 1 and 3, which corresponded to a dominant synoptic-scale
 300 circulation (SD). Group 2 can be considered a mixture of local and synoptic-scale circulation
 301 (MD). These results indicate that Seosan may experience frequent LD conditions (with sun on
 302 one third of the days of the year), with infrequent SD conditions (one fifth of all days).

303

304 **4.2.1 Relationship between daily mean PC-NO₂ and SI-NO₂ under LD, MD, and SD**

305 **conditions**

306 Scatter diagrams of daytime mean PC-NO₂ and SI-NO₂ measurements at Seosan over the entire
307 1-year period are shown in Fig. 5. Based on the 141 cases, daytime mean values averaged
308 between 1100 and 1700 KST were used to reduce the effect of nocturnal PBLH variation. Other
309 data selection criteria included concurrent PC-NO₂ and SI-NO₂ measurements, with data
310 acquisition rates of >80% per day. Overall, PC-NO₂ and SI-NO₂ were strongly correlated ($R =$
311 0.73 ; Fig. 5), suggesting that the vertical profiles were generally uniform in the PBL throughout
312 all four seasons. The slope of the linear regression curve shown in Fig. 5a was 0.02 DU/ppb ($=$
313 $0.53 \times 10^{15} \text{ molecules cm}^{-2}/\text{ppb}$), which is comparable to values ($0.3\text{--}0.59 \times 10^{15} \text{ molecules}$
314 $\text{cm}^{-2}/\text{ppb}$) obtained previously in a study of surface and OMI-NO₂ measurements downwind
315 of strong point sources in Israeli cities (Boersma *et al.*, 2009). The intercept (0.17 DU) was
316 within the range of previous Anmyeondo Pandora measurements, suggesting that intercepts of
317 $0.15\text{--}0.2 \text{ DU}$ may represent the local background PC-NO₂ amount (including the stratospheric
318 NO₂), rather than the influence of local anthropogenic NO₂ emissions.

319 We classified daily averaged PC-NO₂ and SI-NO₂ data according to the three
320 meteorological conditions (LD, MD, and SD) and detected a weak correlation under LD
321 conditions (Fig. 5b); the lowest coefficient of determination for the LD condition ($R^2 = 0.34$)
322 was approximately half of those for the MD (0.359) and SD (0.64) conditions, suggesting that
323 NO₂ vertical profiles were more complex under LD conditions, with anomalous layers.

324

325 **4.2.2 Diurnal variation in column-surface NO₂ under LD, MD, and SD conditions**

326 Diurnal patterns of PC-NO₂, SI-NO₂, and O₃ under SD, MD, and LD conditions are shown in
327 Fig. 6. Under LD conditions, PC-NO₂ increased from morning to afternoon (Fig. 6a), whereas
328 under SD conditions, it had a weak morning peak and subsequent decrease until late afternoon
329 (Fig. 6c). Under MD conditions, PC-NO₂ had one large peak in the morning and a shoulder

330 peak in the late afternoon (Fig. 6b). However, SI-NO₂ showed nearly identical diurnal patterns
331 among the three meteorological conditions, with an early morning peak followed by a second
332 peak in the late afternoon (Fig. 6d–f). Diurnal patterns of O₃ were strongly associated with O₃-
333 NO₂ photochemical reactions under both LD and MD conditions (Fig. 6g–h), whereas no
334 particular photochemical effects were detected under SD conditions (Fig. 6i).

335 A simple linear regression was applied to daytime average (1100–1700 LST)
336 measurements of both PC-NO₂ and SI-NO₂ under the three meteorological conditions, and
337 yielded correlation coefficients (*R*) of 0.51 and 0.41 for SD and MD conditions, respectively;
338 however, LD conditions produced a significantly lower *R* (0.27). Thus, under SD conditions,
339 strong synoptic winds suppressed PC-NO₂ and SI-NO₂ diurnal fluctuations, rendering them
340 similar to each other. Strong winds also inhibited local effects of O₃ formation on the diurnal
341 variation in PC-NO₂, and the smaller impact of chemical conversion from local NO₂ to O₃
342 lowered *R* values during the day. Under MD conditions, both PC-NO₂ and SI-NO₂ exhibited
343 distinctive peaks in the morning with a degree of time lag; both subsequently declined toward
344 noon, and showed higher *R* values than those obtained under SD conditions. By contrast, under
345 MD conditions, correlations were enhanced due to a minimum around 1500 KST for both PC-
346 NO₂ and SI-NO₂, despite time lags in both peaks in the morning and afternoon.

347 Previous studies of the Megacity Air Pollution Seoul (MAPS-Seoul) and KORUS-AQ
348 campaigns reported a typical pattern of continuously increasing PC-NO₂ over the Seoul
349 metropolitan area (Chong *et al.*, 2018; Herman *et al.*, 2018). However, in the current
350 campaign, we found similar results only under LD conditions. The diurnal patterns reported in
351 previous studies were mainly caused by the dominance of NO₂ emissions sources over NO₂
352 losses (Chong *et al.*, 2018; Herman *et al.*, 2018) among several processes associated with NO₂
353 photochemical loss, including transport and deposition, which were also investigated in
354 specific cases in the current study.

355 In this study, we extended the correlation analysis, and investigated the correlation
356 between hourly PC-NO₂ and SI-NO₂ data. The results show a lower correlation in the morning,
357 and a higher correlation in the afternoon (Fig. S1). The respective median correlation
358 coefficients for the LD, MD, and SD meteorological conditions were -0.71, 0.18, and 0.22 in
359 the morning (0900–1200 LST), and 0.84, 0.77, and 0.79 in the afternoon (1200–1400 LST).
360 These values may reflect PBL development. SI-NO₂ decreases in the morning due to the rapid
361 growth of the PBL, while PC-NO₂ increases due to the accumulation of NO₂ in the atmosphere,
362 deriving a lower correlation. However, there is very little change in the PBL in the afternoon,
363 and PC-NO₂ and SI-NO₂ show similar changes, yielding a positive correlation each other
364 during the GMAP-2020 campaign.

365

366 **4.3 Aircraft measurements collected during GMAP-2020**

367 Data collected via aircraft during GMAP-2020 are summarized in Table 2. A total of nine
368 aircraft measurements were conducted during the campaign period (November 12, 2020–
369 January 20, 2021). Four of nine flights were conducted under LD conditions, and the remaining
370 flights (except that on November 27, 2020) were conducted under MD conditions. No aircraft
371 measurements were consistent with SD conditions during the GMAP-2020 campaign.

372 We examined spiral segments from each flight over Seosan during 1100–1700KST to
373 exclude marginal effects of diurnal variation in NO₂ (Fig. 2). The overall results indicated that
374 the vertical O₃ profiles were relatively constant in the PBL, whereas NO₂ profiles appeared to
375 be highly dependent on meteorological conditions. We compared data collected during flights
376 conducted under LD (one flight) and MD conditions (two flights) during the GMAP-2020
377 campaign, to examine differences in the vertical structures of the PA and SI observations.
378 Aircraft measurements of vertical NO₂ and O₃ profiles for flights FL-5 (December 6) and FL-
379 6 (December 8) under LD conditions are shown in Fig. 7, along with 24 h backward trajectories

380 starting at different altitudes (100, 500, and 1,000 m). All observed NO₂ profiles shown in Fig.
381 7 appeared to have generally exponential curves, with anomalous features at higher altitudes.
382 For example, when vertical turbulent mixing prevailed within the PBL (O₃ profile, Fig. 7b),
383 the data were fitted with an exponential vertical curve, and the anomalous NO₂ layer aloft was
384 found to have a height of 1.5 km, which was higher than the estimated PBLH of 1.2 km.
385 HYSPLIT 24 h backward trajectories starting at 1200 KST showed that all air mass from the
386 surface to the lower free atmosphere was transported over the Yellow Sea via the Shandong
387 Peninsula (Fig. 7c). This finding suggests that the anomalous NO₂ layer aloft was not produced
388 locally (i.e., from local LPS emissions), but instead traveled via long-range regional-scale
389 transport. This transport of NO₂ across the region was also discussed and might be particularly
390 high during the winter when the NO_x lifetime is relatively longer (Stohl *et al.*, 2002; Wenig *et*
391 *al.*, 2003; Lee *et al.*, 2013). According to Anmyeondo Lidar measurements for December 6
392 (<http://kalion.kr>), the anomalous NO₂ layer aloft corresponded well to an aerosol layer that
393 appeared at ~1.0 km at approximately 1200 KST, persisting until 2200 KST. However, based
394 on a cross-comparison of our data, high surface levels of SI-NO₂ (> ~4 ppb; Fig. 7a) were
395 influenced more by local LPS than by that in the atmosphere aloft due to long-range transport
396 (Fig. 7a).

397 Aircraft measurements for flight FL-7 (December 9) under LD conditions are shown in
398 Fig. 7b. The NO₂ vertical profile exhibited an exponential curve, with an anomalous peak at
399 ~600 m immediately above the top of the simulated PBL. HYSPLIT backward trajectory data
400 starting at 1200 KST showed that the non-surface air had a different origin from the surface air
401 (Fig. 6d), indicating that the anomalous NO₂ plume likely traveled from coal-fired power plants
402 in a nearby industrial city (Taean) northwest of Seosan. This finding indicates a distinct vertical
403 structure of higher NO₂ at the surface due to strong local emissions, whereas lower NO₂ levels
404 were observed at higher altitudes, with anomalously high NO₂ levels in some layers aloft due

405 to medium-range transport from nearby areas. Thus, despite the limited number of aircraft
406 measurements, the elevated anomalous NO₂ structure that was observed intermittently led to a
407 negative correlation between PA-NO₂ and SI-NO₂. The discrepancies imply that vertical
408 profile distribution study should proceed cautiously when only surface measurements are
409 obtained under LD meteorological conditions.

410 Aircraft measurements were conducted under MD conditions on flights FL-1 (November
411 26), FL-3 (November 28), and FL-8 (December 12) (Fig. 8). We applied several regression
412 models (linear, exponential, and polynomial) to three vertical structures, and obtained two
413 distinct NO₂ vertical profile patterns from the surface to the PBLH: decreasing linearly for FL-
414 1 and FL-8 (Fig. 8), and constant with altitude for FL-3 (Fig. 8b). None of the three cases
415 showed anomalous layers above the PBLH, similar to the exponentially declining profiles
416 obtained under LD conditions (Fig. 7). These vertical structures observed under MD conditions
417 may have been induced by strong vertical mixing within the PBL, supplemented by prominent
418 surface photochemical losses at the same time. The vertical O₃ profile during FL-1 showed a
419 decoupled structure, with different patterns within and above the PBL (Fig. 8d); however, the
420 other 2 days showed uniform distributions, with no particular anomalous features between the
421 upper PBL and surface atmosphere (Fig. 8b, c, e, f). The observed daily maximum sensible
422 heat fluxes measured at Seosan (Fig. S3) were much higher for FL-3 (175.9 Wm⁻²) than FL-1
423 and FL-8 (118.9 and 102.0 Wm⁻²), suggesting that vertical turbulent mixing was much more
424 prominent during FL-3. These chemical and physical characteristics are all related to MD
425 conditions. Thus, the higher coefficient of determination ($R^2 = 0.64$) obtained under MD
426 conditions (Fig. 5b) has an important bearing on the absence of irregular or anomalous layers
427 aloft, with little variation regardless of the shape of the curve (Figs. 7 and 8).

428

429 **4.4 Analyses of column–surface relationships for specific GMAP-2020 cases**

430 Figure 9 shows examples of PC-NO₂ and SI-NO₂ diurnal variation under LD (FL-5 and FL-7)
431 and MD (FL-1 and FL-8) conditions, and Fig. 10 shows latitudinal mean distributions for FL-
432 5 and FL-7, based on the aircraft measurement data shown in Figs. 7 and 8. PC-NO₂ was
433 decoupled from SI-NO₂ on 2 days, FL-5 and FL-7, which were both classified as having LD
434 conditions (Fig. 9a, b), whereas good vertical mixing and uniform NO₂ distribution were
435 observed on the remaining 2 days, FL-1 and FL-8, which showed MD conditions (Fig. 9c, d).
436 According to our analysis of the aircraft measurements (Fig. 7), the poor correlations between
437 PC-NO₂ and SI-NO₂ captured by FL-5 and FL-7 were mainly due to an NO₂ polluted layer
438 transported aloft, as described in Section 4.3.

439

440 **4.4.1 LD conditions**

441 Several cases showed poor correlations between PC-NO₂ and SI-NO₂ under LD conditions
442 within the study period. When we examined the results of previous studies (Thompson et al.,
443 2019; Chong et al., 2018; Herman et al., 2018; Kim et al., 2021), we first considered the
444 possibility that LPS emissions influenced downwind regions under LD conditions, because the
445 increase in PC-NO₂, but not SI-NO₂, may have required an additional source of NO₂ apart from
446 early afternoon traffic emissions. The FL-5 data for December 6 represent an example of this,
447 showing a poor correlation between PC-NO₂ and SI-NO₂ ($R^2 = 0.06$; Fig. 9a). On the same day,
448 Anmyeondo LIDAR detected two elevated aerosol layers at 1200 and 1600–2200 KST
449 (<http://kalion.kr>); the first aerosol layer may reflect a PC-NO₂ peak, as shown in Fig. 9a. The
450 HYSPLIT backward trajectories, starting at different altitudes from the surface to the lower
451 troposphere, revealed that all air parcels moved eastward from China to Anmyeondo and
452 Seosan (Figure 1); thus, other NO₂ plumes may have begun to pass over Seosan at 1600KST
453 (Fig. 7c). Longitudinal SI-NO₂ distributions (Fig. 10) exhibited 5.2 ppb at 126.1°E, 8.1 ppb at
454 126.3°E, and 7.3 ppb at 126.4°E, averaged between 1300 and 1600 KST by longitude (Table

455 S1), whereas they were nearly constant at a height of 500–600 m on December 6. Therefore,
456 westerly winds advected cleaner air from Padori (AQM₁) to Seosan at the surface, but not at a
457 height of 500–600 m, contributing to low SI-NO₂ levels in the afternoon (Fig. 9a).

458 Another example of a weak correlation was obtained by flight FL-7 (December 9), as
459 shown in Fig. 9b. Time series PC-NO₂ data exhibited several peaks during 1200–1400 KST
460 (Fig. 9b), whereas SI-NO₂ showed less temporal variation, resulting in a weak correlation ($R =$
461 -0.24) compared to the overall daytime (1100–1700 KST) correlation ($R^2 = 0.53$; Fig. 5a).
462 Latitudinal NO₂ levels at high altitudes of ~600 m (Fig. 10b) gradually increased northward,
463 whereas surface NO₂ was minimal at the midpoint. For example, at high altitudes, the
464 latitudinal mean NO₂ levels were 1.4 ppb (36.8°N), 4.1 ppb (36.9°N), and 5.1 ppb (37.0°N),
465 whereas the SI-NO₂ levels at the same sites were 18.0 ppb (36.8°N), 14.3 ppb (36.9°N), and
466 16.8 ppb (37.0°N), respectively, averaged during 1200–1400 KST by latitude (Table S1). This
467 finding is attributable to a prevailing north wind that transported NO₂ southward at high
468 altitudes, while simultaneously ventilating SI-NO₂ toward outer Seosan, resulting in the
469 development of several PC-NO₂ peaks. By contrast, SI-NO₂ decreased slowly (Figs. 9b and
470 10b).

471

472 **4.4.2 MD and SD conditions**

473 We obtained higher PC–SI correlation coefficients under MD and SD conditions than LD
474 conditions (Figs. 5b and 9c, d). Under MD and SD conditions, diurnal variation in PC-NO₂ and
475 SI-NO₂ showed simultaneous declines from early morning until noon (Fig. 6). Notably, PC-
476 NO₂ showed a continuously decreasing trend, particularly during the morning hours, in the
477 period of approximately 0900–1200 KST under both MD and SD conditions (Fig. 6b, c). These
478 diurnal patterns of decreasing PC-NO₂ in the study area were opposite to those reported in
479 previous studies (Chong *et al.*, 2018; Herman *et al.*, 2018) that observed increasing PC-NO₂ in

480 large urban areas during the daytime, caused by higher NO₂ emissions even during
481 photochemical NO₂ losses to form O₃.

482 We hypothesized that decreasing PC-NO₂ can occur due to photochemical loss and
483 surface wind transport, which both intensify with increasing solar radiation in the morning.
484 Photochemically, NO₂ is converted into photochemical oxidants such as PAN, HNO₃, and
485 nitrate under sunlight, thereby disrupting the NO_x-VOC-O₃ cycle. Concurrently, W_{sf}
486 intensified due to thermal turbulence transport of NO₂ emissions away from Seosan during the
487 day. Thus, PC-NO₂ decreases under MD conditions as a result of ventilation effects caused by
488 stronger wind speeds. There are two possible mechanisms for this: sea breeze penetration
489 (because the study area is adjacent to the northern coast of the Taean Peninsula; Fig. 1) and
490 vigorous turbulent mixing (which leads to vertical mixing of surface NO₂ during PBL growth;
491 Sun *et al.*, 2013). We investigated these factors in detail for specific cases.

492 Figure 11 shows the diurnal variation in selected meteorological and chemical variables
493 measured under MD (November 25) and SD conditions (December 14). Under MD conditions
494 (Fig. 11a–c), declines in PC-NO₂ and SI-NO₂ were observed toward noon. In particular,
495 decreasing PC-NO₂ was accompanied by increased W_{sf} (Fig. 11b); therefore, we examined
496 GMAP-2020 campaign measurements of sea breeze penetration. Figure S2a shows diurnal
497 variation in observed air temperatures at site Met₁ and measured sea surface temperatures at
498 nearby site Met₂ (37.14°N, 126.01°E), located 55 km from PA₄. The thermal meteorological
499 observations were used to calculate SBI (+0.37), which was greater than +3 (the threshold for
500 sea breeze occurrence; Brigges and Graves, 1962). Sea breeze disturbances with a sharp
501 decrease (increase) in temperature (humidity) were observed at site Met₃ (Fig. S3b), which is
502 located on the northern coastline of Taean Peninsula (Fig. 1). However, sea breezes did not
503 progress inland at the Met₁ Seosan Meteorological Automated Surface Observing System
504 (ASOS) site, which is closer to the Pandora sites; sea breezes did not correlate with NO₂

505 ventilation to offset its high emission.

506 We further detected a strong positive correlation between wind speed and sensible heat
507 flux (Fig. 11b). We speculated that thermal and momentum turbulences caused by a vertical
508 temperature gradient and surface friction entrained surface turbulence, thus increasing
509 momentum in the free atmosphere downward to the surface due to strong turbulent mixing
510 within the PBL, in turn leading to a uniform vertical NO₂ profile with a positive correlation
511 between PC-NO₂ and SI-NO₂. Figure S3 shows a comparison of daily maximum sensible heat
512 and momentum fluxes under LD, MD, and SD conditions during the GMAP-2020 campaign.
513 SD conditions showed the highest mean heat flux, followed by MD and LD, indicating that
514 downward momentum transport led by both heat and momentum fluxes plays a greater role in
515 Wsfc enhancement under MD than LD conditions within the PBL.

516 Photolytic NO₂ loss was detected as temporal variation in NO₂, NO₃⁻, and CO at PA₄.
517 Because no NO₂ analyzer was installed at PA₄, NO₂^{*}(= NO_y-NO) was used instead of NO₂
518 under the assumption that NO_z is negligible in winter. Figure 11c shows the diurnal variation
519 in NO₂, O₃, and NO₃⁻ under MD conditions, normalized by CO to reduce the effect of PBL
520 evolution. The results showed that NO₂/CO decreased after the morning peak; however, NO₃⁻
521 /CO and O₃/CO increased toward midday, indicating that photolytic activity also contributed
522 considerably to the concurrent decline of SI-NO₂ and PC-NO₂ (Fig. 11a). In turn, this indicated
523 that photochemistry can contribute to higher correlation coefficients under MD conditions.

524 Under SD conditions (Fig. 11d-f), PA-NO₂ and SI-NO₂ exhibited weak diurnal variability
525 compared to LD and MD conditions. SD conditions on December 14 produced significantly
526 stronger winds (i.e., wind speed > 6 m s⁻¹ at 1300 KST), with generally higher PBLHs (Fig.
527 11e). Meteorological features, such as strong wind at both 850 hPa (18.0 m s⁻¹) and 10 m height
528 (4.26 m s⁻¹), suppressed both PC-NO₂ and SI-NO₂ (7.3 ppb and 0.31 DU, respectively) to
529 below the average, producing a strong correlation ($R = 0.9$ at AQM₅) and nearly flattening their

530 temporal curves during the day (Fig. 11d). Thus, under SD conditions, wind speed and
531 turbulent fluxes such as sensible heat flux had larger values, and NO_2 and NO_3^- decreased or
532 increased at the same time during the day (Fig. 11f), indicating that the transport effect was
533 much greater than that of local photochemical loss over the study area.

534 In conclusion, in this case-specific study, we assessed the correlations between PC- NO_2
535 and SI- NO_2 , and explored their mechanisms by investigating the impact of meteorological and
536 photochemical conditions. A weak correlation between PC- NO_2 and SI- NO_2 occurred when
537 anomalously high concentrations remained, with ragged fragments of NO_2 plumes in the upper
538 or middle layers. We also found that a negative correlation occurred intermittently under LD
539 conditions, with generally lower PBLH. In particular, elevated pollutant levels due to regional-
540 scale transport or decoupled NO_2 plumes advected within the PBL may have also caused the
541 weak correlation between PC- NO_2 vs. SI- NO_2 . These phenomena were detected only from the
542 PA-SI coupled measurements in this study. Thus, when either PC or SI observations are
543 applied alone for understanding the vertical structure of air pollutants, undetected bias can
544 occur under LD conditions, particularly where transport processes prevail, and these results
545 can be also applicable to GEMS observations analysis.

546

547 **5. Conclusion**

548 We explored the potential applicability of combined PC- NO_2 and SI- NO_2 measurements
549 collected at Seosan during the GMAP-2020 campaign. We characterized the correlation
550 between PC- NO_2 and SI- NO_2 under various conditions to understand the complex air quality
551 of Seosan, which appears to be vulnerable to LPS emissions from surrounding areas. We
552 hypothesize that correlations between PC- NO_2 and SI- NO_2 are closely related to NO_2 vertical
553 profiles, which also depend on meteorological conditions. We performed statistical analyses of
554 a year-long PC- NO_2 dataset (November 12, 2020–October 30, 2021) combined with

555 meteorological data, *in situ* ground data, and airborne chemical data measured during the
556 GMAP-2020 campaign in the same period.

557 Our results show that hourly PC-NO₂ and SI-NO₂ over the 1-year period exhibited a linear
558 relationship with a fair correlation ($R = 0.41$), and daily mean PC-NO₂ vs. SI-NO₂ exhibited a
559 good linear correlation ($R = 0.73$), supporting the overall uniformity of NO₂ profiles in the PBL
560 over Seosan despite the continuous impact of LPS emissions.

561 The impact of meteorological conditions on the relationship between PC-NO₂ and SI-NO₂
562 was investigated through agglomerative hierarchical clustering, which indicated three
563 meteorological conditions: LD, MD, and SD. Under LD conditions, southerly winds advect
564 warm air under the upper ridge, forming stable and short PBLs and weak surface winds. By
565 contrast, under SD conditions, cold northerly winds induce unstable and high PBLs with strong
566 surface winds. The correlations between daily mean PC-NO₂ and SI-NO₂ levels, and their
567 variation during 1100–1700 KST, weakened under LD conditions, suggesting that the shape of
568 the NO₂ profile typically deviates from a uniform profile under SD and MD conditions. Aircraft
569 measurements under LD conditions demonstrated NO₂ plumes aloft, with anomalous vertical
570 structures and different horizontal (latitudinal) gradients of surface NO₂ at higher altitudes,
571 such as 600 m over Seosan.

572 Thus, the relationship between PC-NO₂ and SI-NO₂ depends on the presence of NO₂
573 plumes aloft under LD conditions, which provide a favorable environment for LPS plumes
574 decoupled from the surface at Seosan. Our findings suggest that the correlation between PC-
575 NO₂ and SI-NO₂ may serve as an indicator of the degree of complexity of urban air quality.
576 This correlation can be optimally applied for air quality evaluation and vertical analysis by
577 combining the Pandora Asia Network with AQM networks, and the results can be also applied
578 to environmental GEMS observation analysis in combination with SI observations. More
579 detailed studies on urban air pollution evaluation will be undertaken based on PC, DOAS,

580 aircraft, SI air quality, and surface turbulence observation data, as well as modeling studies of
581 data collected during the GMAP-2021 campaign.

582

583 **Acknowledgments**

584 We thank all those who contributed to the GMAP-2020 field campaign, NASA GSFC for use of Pandora
585 instruments, and PGN for raw data processing.

586

587 **Funding.**

588 This study was supported by the National Institute of Environmental Research (NIER-2021-01-01-052
589 and NIER-2021-03-03-001), and was partially supported by National Research Foundation of Korea
590 (NRF) funded by the Ministry of Education of the Republic of Korea (Grant No. 2020R1I1A2075417)

591

592 **Data Availability.**

593 The measurements can be accessed by contacting the corresponding authors.

594

595 **Competing interest.**

596 The authors declare that they have no conflict of interest.

597

598 **Author Contributions.**

599 Lim-Seok Chang: Conceptualization, Formal analysis, Visualization, Investigation, Writing -
600 Original draft; Donghee Kim, Hyunkee Hong, Deok-Rae Kim, Jeonga Yu, and Daewon Kim; Data
601 curation; Hanlim Lee, Kwangyul Lee, and Jinkyu Hong: Methodology and formal analysis; Hyun-
602 Young Jo: Formal analysis and Visualization; Cheol-Hee Kim ; Writing—original draft preparation,
603 Writing—review and editing. All authors have read and agreed to the published version of the
604 manuscript.

605 **References**

- 606 Biggs, W.G. and Graves, M.E.: A lake breeze index, *J. Appl. Meteor.*, 1, 474–480,
607 <http://www.jstor.org/stable/26169480>, 1962.
- 608 Boersma, K.F., Jacob, D.J., Trainic, M., Rudich, Y., DeSmedt, I., Dirksen, R., and Eskes, H.J.:
609 Validation of urban NO₂ concentrations and their diurnal and seasonal variations observed from the
610 SCIAMACHY and OMI sensors using in situ surface measurements in Israeli cities. *Atmos. Chem.*
611 *Phys.*, 9, 3867–3879, <https://doi.org/10.5194/acp-9-3867-2009>, 2009.
- 612 Cede A.: Manual for Blick Software Suite 1.7, Tech. rep., LuftBlick, Austria, 161 pp., 2019.
- 613 Chong, H., Lee, H., Koo, J.H., Kim, J., Jeong, U., Kim, W., Kim, S.W., Herman, J.R., Abuhassan, N.K.,
614 Ahn, J.Y., Park, J.H., Kim, S.K., Moon, K.J., Choi, W.J., and Park, S.S.: Regional characteristics
615 of NO₂ column densities from Pandora observations during the MAPS-Seoul campaign, *Aerosol*
616 *Air Qual. Res.* 18, 2207–2219, <https://doi.org/10.4209/aaqr.2017.09.0341>, 2018.
- 617 Engel-Cox, J.A., Holloman, C.H., Coutant, B.W., and Hoff, R.M.: Qualitative and quantitative
618 evaluation of MODIS satellite sensor data for regional and urban scale air quality, *Atmos. Environ.*,
619 38, 2495–2509, <http://dx.doi.org/10.1016/j.atmosenv.2004.01.039>, 2004.
- 620 Flynn, C.M., Pickering, K.E., Crawford, J.H., Weinheimer, A.J., Diskin, G., Thornhill, K.L., Loughner,
621 C., Lee, P., and Strode, S.A.: Variability of O₃ and NO₂ profile shapes during DISCover-AQ:
622 Implications for satellite observations and comparisons to model-simulated profiles, *Atmos.*
623 *Environ.*, 147, 133–156, <https://doi.org/10.1016/j.atmosenv.2016.09.068>, 2016.
- 624 Herman, J., Cede, A., Spinei, E., Mount, G., Tzortziou, M., and Abuhassan, N.: NO₂ column amounts
625 from ground-based Pandora and MFDOAS spectrometers using the direct-sun DOAS technique:
626 Intercomparisons and application to OMI validation, *J. Geophys. Res. Atmos.*, 114, D13307,
627 <https://doi.org/10.1029/2009JD011848>, 2009.
- 628 Herman, J., Spinei, E., Fried, A., Kim, J., Kim, J., Kim, W., Cede, A., Abuhassan, N., and Rozenhaimer,
629 S.M.: NO₂ and HCHO measurements in Korea from 2012 to 2016 from Pandora spectrometer

630 instruments compared with OMI retrievals and with aircraft measurements during the KORUS-AQ
631 campaign, *Atmos. Meas. Tech.*, 11, 4583–4603, <https://doi.org/10.5194/amt-11-4583-2018>, 2018.

632 Hong, J.-W., Lee, S.-D., Lee, K., and Hong, J.: Seasonal variations in the surface energy and CO₂ flux
633 over a high-rise, high-population, residential urban area in the East Asian monsoon region, *Int. J.*
634 *Climatol.*, 40, 4384–4407, <https://doi.org/10.1002/joc.6463>, 2019.

635 Jo, H.-Y. and Kim, C.-H: Identification of long-range transported haze phenomena and their
636 meteorological features over Northeast Asia, *J. Appl. Meteorol. Climatol.*, 52(6), 1318–1328,
637 <https://doi.org/10.1175/JAMC-D-11-0235.1>, 2013.

638 Kim, C.-H., Lee, H.-J., Kang, J.-E., Jo, H.-Y., Park, S.-Y., Jo, Y.-J., Lee, J.-J., Yang, G.-H., Park, T.,
639 and Lee, T.: Meteorological Overview and Signatures of Long-range Transport Processes during
640 the MAPS-Seoul 2015 Campaign, *Aerosol Air Qual. Res.*, 18, 2173–2184,
641 <https://doi.org/10.4209/aaqr.2017.10.0398>, 2018.

642 Kim, C.-H., Park, S.-Y., Kim, Y.-J., Chang, L.-S., Song, S.-K., Moon, Y.-S., and Song, C.-K.: A
643 Numerical Study on Indicators of Long-range Transport Potential for Anthropogenic Particle Matter
644 over Northeast Asia, *Atmos. Environ.*, 58, 35–44, <https://doi.org/10.1016/j.atmosenv.2011.11.002>,
645 2012.

646 Kim, J., Jeong, U., Ahn, M.-H., Park, R.J., Lee, H., Song, C.H., Choi, Y.-S., Lee, K.-H. Yoo, J.-M.,
647 Jeong, M.-J. Park, S.K., Lee, K.-M., Song, C.-K., Kim, S.-W., Kim, Y.J., Kim, S.-W., Kim, M., Go,
648 S., Liu, X., Chance, K., Miller, C.C., Al-Saadi, J., Veihelmann, B., Bhartia, P.K., Torres, O., Abad,
649 G.G., Haffner, D.P., Ko, D.H., Lee, S.H., Woo, J.-H., Chong, H., Park, S.S., Micks, D., Choi, W.J.,
650 Moon, K.-J., Veefkind, P., Levelt, P.F., Edwards, D.P., Kang, M., Eo, M., Bak, J., Baek, K., Kwon,
651 H.-A., Yang, J., Park, J., Han, K.M., Kim, B.-R., Shin, H.-W., Choi, H., Lee, E., Chong, J., Cha, Y.,
652 Koo, J.-H., Hayashida, S., Kasai, Y., Kanaya, Y., Liu, C., Lin, J., Crawford, J.H., Carmichael, G.R.,
653 Newchurch, M.J., Lefer, B.L., Herman, J.R., Swap, R.J., Lau, A.K.H., Kurosu, T.P., Jaross, G.,
654 Ahlers, B., Dobber, M., McElroy, T.C., and Choi, Y.: New era of air quality monitoring from space:

655 Geostationary Environment Monitoring Spectrometer (GEMS), *Bulletin of the American*
656 *Meteorological Society*, 101(1), E1-E22, <https://doi.org/10.1175/BAMS-D-18-0013.1>, 2020.

657 Kim, S.-U., Kim, K.-Y.: Physical and chemical mechanisms of the daily-to-seasonal variation of PM₁₀
658 in Korea. *Sci. Total Environ.*, 712, 136429, <https://doi.org/10.1016/j.scitotenv.2019.136429>, 2020.

659 Kim, S.-M., Koo, J.-H., Lee, H., Mok, J., Choi, M., Go, S., Lee, S., Cho, Y., Hong, J., and Seo, S.:
660 Comparison of PM_{2.5} in Seoul, Korea Estimated from the Various Ground-Based and Satellite AOD,
661 *Appl. Sci.*, 11(22), 10755, <https://doi.org/10.3390/app112210755>, 2021.

662 Lamsal, L.N., Martin, R.V., van Donkelaar, A., Celarier, E.A., Bucsela, E.J., Boersma, K.F., Dirksen,
663 R., Luo, C., and Wang, Y.: Indirect validation of tropospheric nitrogen dioxide retrieved from the
664 OMI satellite instrument: Insight into the seasonal variation of nitrogen oxides at northern
665 midlatitudes, *J. Geophys. Res.*, 115, D05302, <https://doi.org/10.1029/2009JD013351>, 2010.

666 Lee, S., Kim, M., Kim, S.Y., Lee, D.W., Lee, H., Kim, J., Le, S., and Liu, Y.: Assessment of long-range
667 transboundary aerosols in Seoul, South Korea from Geostationary Ocean Color Imager (GOCI) and
668 ground-based observations, *Environ. Pollut.*, 269, 115924,
669 <https://doi.org/10.1016/j.envpol.2020.115924>, 2021.

670 Lee, S.J., Lee, J., Greybush, S.J., Kang, M., and Kim, J.: Spatial and temporal variation in PBL height
671 over the Korean Peninsula in the KMA operational regional model, *Adv. Meteorol.*, 2013(10), 1-
672 16, <https://doi.org/10.1155/2013/381630>, 2013.

673 National Institute of Environmental Research (NIER): Air Quality Monitoring Network Installation and
674 Operation. Ministry of the Environment, Seoul, Korea, 2021.

675 Sanchez, M.L., Pascual, D., Ramos, C. and Perez, I.: Forecasting particulate pollutant concentrations in
676 a city from meteorological variables and regional weather patterns, *Atmos. Environ.*, 6, 1509–1519,
677 [https://doi.org/10.1016/0960-1686\(90\)90060-Z](https://doi.org/10.1016/0960-1686(90)90060-Z), 1990.

678 Stohl, A., Eckhardt, S., Forster, C., James, P., and Spichtinger, N.: On the pathways and timescales of

679 intercontinental air pollution transport, *J. Geophys. Res.*, 107(D23), 4684,
680 doi:10.1029/2001JD001396, 2002.

681 Sun, J., Lenschow, D.H., Mahrt, L., and Nappo, C.: The relationships among wind, horizontal pressure
682 gradient, and turbulent momentum transport during CASES-99, *J. Atmos. Sci.*, 70, 3397–3414,
683 <http://dx.doi.org/10.1175/JAS-D-12-0233.1>, 2013.

684 Thompson, A.M., Stauffer, R.M., Boyle, T.P., Kollonige, D.E., Miyazaki, K., Tzortziou, M., Herman,
685 J.R., Abuhassan, N., Jordan, C.E., and Lamb, B.T.: Comparison of near-surface NO₂ pollution with
686 Pandora total column NO₂ during the Korea-United States Ocean Color (KORUS OC) Campaign,
687 *J. Geophys. Res. Atmos.*, 124, 13560–13575, <https://doi.org/10.1029/2019JD030765>, 2019.

688 Van Roozendaal, M. and Fayt, C.: WinDOAS Software user manual, Tech. rep., IASB/BIRA, Uccle,
689 Belgium, <http://uv-vis.aeronomie.be/software/WinDOAS>, 2001.

690 Venkat Reddy M., Vivekananda M. and Satish RUVN: Divisive Hierarchical Clustering with K-means
691 and Agglomerative Hierarchical Clustering, *International Journal of Computer Science Trends and*
692 *technology*, 5(5), 6–12, doi:10.17485/ijst/2016/v9is1/96012, 2017.

693 Wang, J., and Christopher, S.A.: Intercomparison between satellite-derived aerosol optical thickness
694 and PM_{2.5} mass: Implications for air quality studies, *Geophys. Res. Lett.*, 30, 2095,
695 <https://doi.org/10.1029/2003GL018174>, 2003.

696 Wang, Y., Dörner, S., Donner, S., Böhnke, S., Smedt, I.D., Dickerson, R.R., Dong, Z., He, H., Li, Z.,
697 Li, D., Ren, X., Theys, N., Wang, Y., Wang, Z., Xu, H., Xu, J., and Wagner, T.: Vertical profiles of
698 NO₂, SO₂, HONO, HCHO, CHOCHO and aerosols derived from MAX-DOAS measurements at a
699 rural site in the central western North China Plain and their relation to emission sources and effects
700 of regional transport, *Atmos. Chem. Phys.*, 2, 5417–5449, [http://dx.doi.org/10.5194/acp-19-5417-](http://dx.doi.org/10.5194/acp-19-5417-2019)
701 2019, 2019.

702 Wenig, M., Spichtinger, N., Stohl, A., Held, G., Beirle, S., Wagner, T., Jahne, B., and Platt, U.:
703 Intercontinental transport of nitrogen oxide pollution plumes, *Atmos. Chem. Phys.*, 3, 387–393,

704 SRef-ID: 1680-7324/acp/2003-3-387, 2003.

705 Zhao, X., Griffin, D., Fioletov, V., McLinden, C., Davies, J., Ogyu, A., Lee, S. C., Lupu, A., Moran,
706 M. D., Cede, A., Tiefengraber, M., and Müller, M.: Retrieval of total column and surface NO₂ from
707 Pandora zenith-sky measurements, *Atmos. Chem. Phys.*, 19, 10619–10642,
708 <https://doi.org/10.5194/acp-19-10619-2019>, 2019.

709

710

711

712

713

714

715

716

717

718

719

720

721

722

723

List of Tables

724
725
726
727
728
729
730
731
732
733
734
735
736
737
738
739
740
741
742

Table 1. Summary of NO₂ column data from four Pandora (PA) measurement sites.

Table 2. Summary of aircraft measurements collected during the Geostationary Environment Monitoring Spectrometer (GEMS) Map of Air Pollution (GMAP)-2020 campaign period (November 12, 2020–January 20, 2021).

Table 1. Summary of NO₂ column data from four Pandora (PA) measurement sites.

Site	Site name	Site location		Mean (DU)	SD (DU)	Minimum (DU)	Maximum (DU)	Number of data points (days)	Operating period
		Longitude (°E)	Latitude (°N)						
PA ₁	Seosan-DHJ	126.502	36.900	0.50	0.22	0.20	1.60	838 (11)	GMAP-2020 campaign
PA ₂	Seosan-DM	126.458	36.778	0.43	0.19	0.18	1.62	1241 (13)	GMAP-2020 campaign
PA ₃	Seosan-CC	126.449	36.785	0.40	0.14	0.18	0.97	1242 (13)	GMAP-2020 campaign
PA ₄	Seosan-SS	127.492	36.777	0.39	0.16	0.17	1.79	8753 (141)*	1 year (Nov. 12, 2020–Oct. 30, 2021)

* The Pandonia Global Network (PGN) retrieval algorithm was applied to yearly measurements.

743

744 **Table 2.** Summary of aircraft measurements collected during the Geostationary Environment
745 Monitoring Spectrometer (GEMS) Map of Air Pollution (GMAP)-2020 campaign period
746 (November 12, 2020–January 20, 2021).

Flight no.	Date	Meteorological classification
FL-1	Nov. 26, 2020	MD ¹⁾
FL-2	Nov. 27, 2020	No Pandora measurements
FL-3	Nov. 28, 2020	MD
FL-4	Dec. 1, 2020	LD ²⁾
FL-5	Dec. 6, 2020	LD
FL-6	Dec. 8, 2020	LD
FL-7	Dec. 9, 2020	LD
FL-8	Dec. 12, 2020 (am)	MD
FL-9	Dec. 12, 2020 (pm)	MD

747 ¹⁾ LD: local wind-dominant conditions; ²⁾ MD: mixed conditions.

748

749

750

751

752

Figure Captions

753 **Figure 1.** Map of sites used for Geostationary Environment Monitoring Spectrometer (GEMS) Map of
754 Air Pollution (GMAP) campaigns conducted in (left) Seosan, South Korea in November 2020 to
755 January 2021 (GMAP-2020), and (right) the Seoul metropolitan area from October 2021 to November
756 2021 (GMAP-2021). (Left) Measurement sites around Seosan, the study area for the GMAP-2020
757 campaign. Red circles indicate Pandora column measurement sites including (left) Seosan Daehoji
758 (PA₁), Seosan Dongmun (PA₂), Seosan City Council (PA₃), and Seosan Super Site (PA₄). Blue triangles
759 indicate large point sources (LPSs) including the Taeon and Dangjin thermal power stations (LPS₁ and
760 LPS₂, respectively), Hyundai steelworks (LPS₃), and Daesan petrochemical complex (LPS₄). Yellow
761 squares indicate Automated Synoptic Observing System meteorological sites in Seosan (Met₁), AWS
762 (Met₂), and buoy (Met₃). Green squares indicate air quality monitoring (AQM) network stations
763 including Padori (AQM₁), Leewon (AQM₂), Taeon (AQM₃), Daesan (AQM₄), Seongyeon (AQM₅), and
764 Dongmoon (AQM₆). In the right panel, the black line indicates the route used for car-based differential
765 optical absorption spectroscopy (Car-DOAS) measurements and the blue dotted line indicates the
766 horizontal domain of Geo-CAPE airborne simulator (GCAS) measurements taken during the GMAP-
767 2021 campaign.

768

769 **Figure 2.** Flight tracks for two Cessna Grand Caravan 208 B aircraft over Pandora sites (left)
770 PA₄ and (right) PA₁ during the GMAP-2020 campaign. Colored circles indicate airborne NO₂
771 concentration observations. Stacked circles indicate spiral flights conducted over two sites.

772

773 **Figure 3.** (a) Pandora column (PC) NO₂ measurements as a function of surface *in situ* (SI) NO₂
774 observations at Pandora sites PA₁–PA₃ during the GMAP-2020 campaign and PA₄ during a 1-
775 year period. A 1:1 linear regression model was used to evaluate the relationship between PC
776 and SI measurements (black line). (b) Samplescatter plots of PC-NO₂ and SI-NO₂ for February
777 24 (red) and April 21 (blue), 2021.

778

779 **Figure 4.** K-means clustering yielded three groups of cases for (a) surface NO₂ and (b) PC-
780 NO₂, associated with eight meteorological variables: (c) surface wind speed (Wsfc), (d) Psfc,
781 (e) Psfc tendency (dPsfc/dt), (f) 925-hPa air temperature (T925), (g) 850-hPa wind speed
782 (W850), (h) 850-hPa north–south wind component (NS850), (i) 850-hPa east–west wind
783 component (EW850), and (j) 500-hPa geopotential height (GPH500). All data were de-

784 seasonalized using the 30-day moving average, except PC-NO₂, for which the monthly average
785 was used. (k) Simulated daily maximum mixing height (not directly clustered). (l) Box and
786 whisker plots of the sea breeze index (SBI) at Seosan for the 1-year period. Red dots indicate
787 the critical SBI (a value of 3), suggested by Biggs and Graves (1962).

788

789 **Figure 5.** (a) Scatterplots of daytime measurements at site PA₄ (a) PC-NO₂ vs. SI-NO₂ under
790 all meteorological conditions and (b) PC-NO₂ vs. Surface Δ NO₂ in each meteorological
791 condition over a 1-year period (November 12, 2020–October 30, 2021). Here Surface Δ NO₂
792 = SI-NO₂–(30-day moving average) SI-NO₂.

793

794 **Figure 6.** Box and whisker plots of diurnal variation in (a–c) PC-NO₂, (d–f) SI-NO₂, and (g–
795 i) surface O₃ under synoptic wind-dominant (SD), mixed (MD), and local wind-dominant (LD)
796 conditions in Seosan during a 1-year period (November 12, 2020–October 30, 2021).

797

798 **Figure 7.** Box and whisker plots of the vertical NO₂ and O₃ profiles measured by GMAP
799 aircraft superposed with *in situ* AQMS₁ measurements during flights (a, b) FL-5 (December 6)
800 and (d, e) FL-7 (December 6 and 9). Blue dashed lines are linear regression lines fitted to NO₂
801 and O₃ profiles within the planetary boundary layer (PBL). Black arrows indicate the simulated
802 PBL height (PBLH) obtained from the Korea Meteorological Administration (KMA).
803 HSYPLIT 24-h backward trajectories in Seosan are shown at altitudes of 100, 500, and 1,000
804 m, starting at 1600 KST on November 26 and 1200 KST on December 12.

805

806 **Figure 8.** Box and whisker plots of vertical profiles obtained from GMAP aircraft superposed
807 with *in situ* AQMS measurements for (1) NO₂ and (2) O₃ for flights (a) FL-1 (November 26),
808 (b) FL-3 (November 28), and (c) FL-8 (December 12). Blue dashed lines are linear regression
809 lines fitted to NO₂ and O₃ in the PBL. Black arrows indicate PBLH simulated by the Hybrid
810 Single-Particle Lagrangian Integrated Trajectory (HYSPLIT) Global Forecast System (GFS).

811

812 **Figure 9.** Time series and scatterplots of PC-NO₂ and SI-NO₂ at PA₂ on (a) December 6, (b)
813 December 9, (c) November 26, and (d) December 12. (e) Scatterplot of PC-NO₂ and SI-NO₂
814 on December 6 (blue), December 9 (red), November 26 (gray), and December 12 (black). (f)
815 Vertical potential temperature profiles on December 6, 9, and 12, 2020. Radiosonde data for
816 November 26, 2020 are missing.

817
818 **Figure 10.** Latitudinal NO₂ distribution at the surface and 600 m over PA₄ (Seosan Super Site),
819 averaged during (a) 1300–1600 KST on December 6 (FL-5) by longitude and (b) 1200–1400
820 KST on December 9 (FL-7) by latitude, obtained from airborne (blue) and surface
821 measurements (red).

822
823 **Figure 11.** Examples of the diurnal variation on November 25 (a, c, e) and December 14 (b, d,
824 f). (a, b) Column NO₂ at sites PA₁–PA₄ and surface NO₂ at air quality monitoring sites AQM₄
825 and AQM₆. (c, d) Sensible heat fluxes and surface wind speed at PA₄. (e, f) Diurnal variation
826 in NO₂, NO₂⁻, and O₃ normalized by CO. Figure 1 shows the locations of the measurement
827 sites.

828

829

830

831

832

833

834

835

836

837

838

839

840

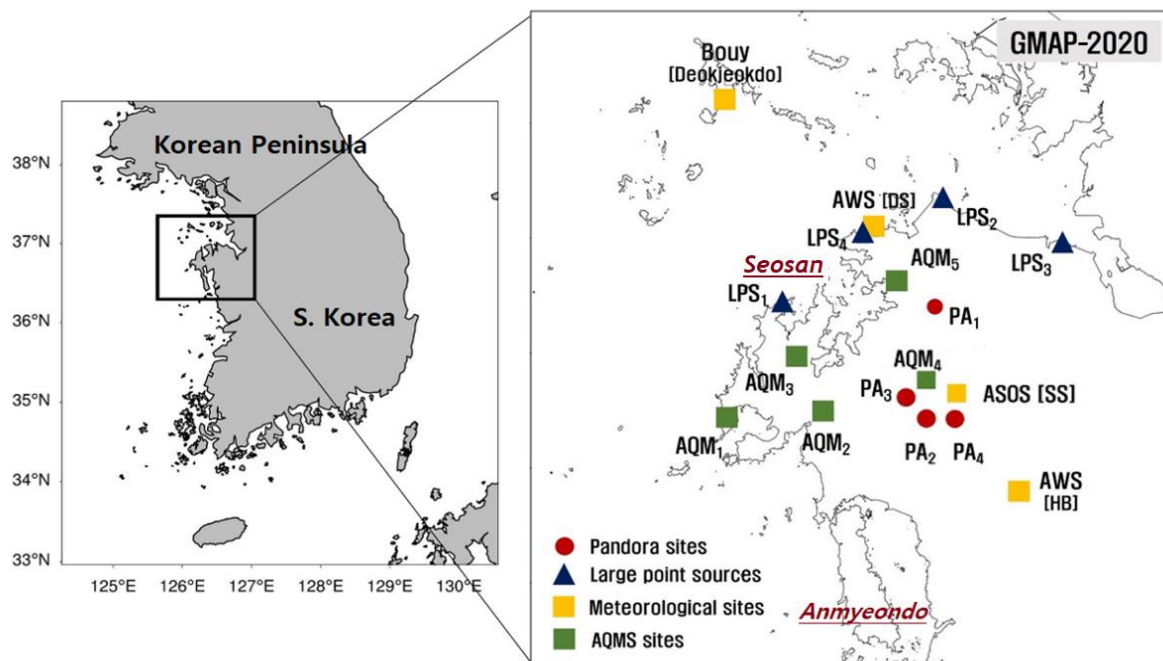
841

842

843

844

845



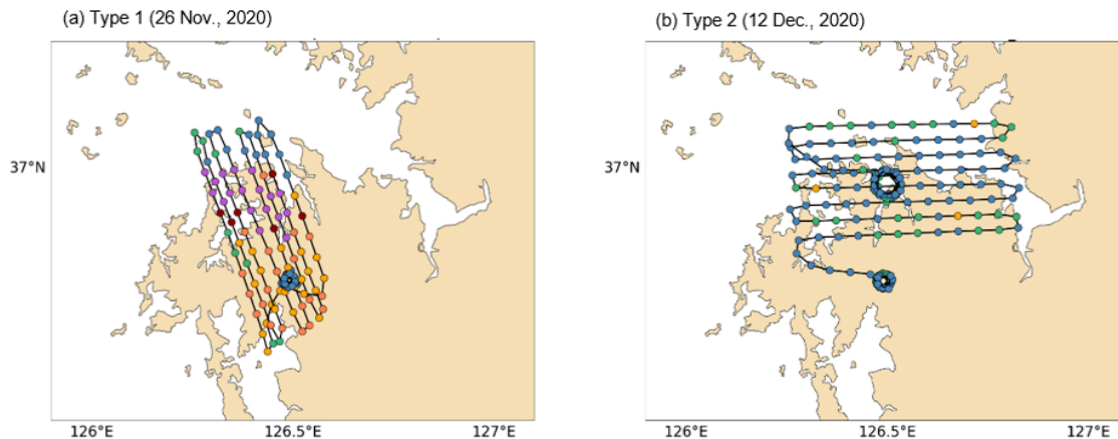
846

847 **Figure 1.** Map of sites used for Geostationary Environment Monitoring Spectrometer (GEMS) Map of
848 Air Pollution (GMAP) campaigns conducted in (left) Seosan, South Korea in November 2020 to
849 January 2021 (GMAP-2020), and (right) the Seoul metropolitan area from October 2021 to November
850 2021 (GMAP-2021). (Left) Measurement sites around Seosan, the study area for the GMAP-2020
851 campaign. Red circles indicate Pandora column measurement sites including (left) Seosan Daehoji
852 (PA₁), Seosan Dongmun (PA₂), Seosan City Council (PA₃), and Seosan Super Site (PA₄). Blue triangles
853 indicate large point sources (LPSs) including the Taean and Dangjin thermal power stations (LPS₁ and
854 LPS₂, respectively), Hyundai steelworks (LPS₃), and Daesan petrochemical complex (LPS₄). Yellow
855 squares indicate Automated Synoptic Observing System meteorological sites in Seosan (Met₁), AWS
856 (Met₂), and buoy (Met₃). Green squares indicate air quality monitoring (AQM) network stations
857 including Padori (AQM₁), Leewon (AQM₂), Taean (AQM₃), Daesan (AQM₄), Seongyeon (AQM₅), and
858 Dongmoon (AQM₆). In the right panel, the black line indicates the route used for car-based differential
859 optical absorption spectroscopy (Car-DOAS) measurements and the blue dotted line indicates the
860 horizontal domain of Geo-CAPE airborne simulator (GCAS) measurements taken during the GMAP-
861 2021 campaign.

862

863

864



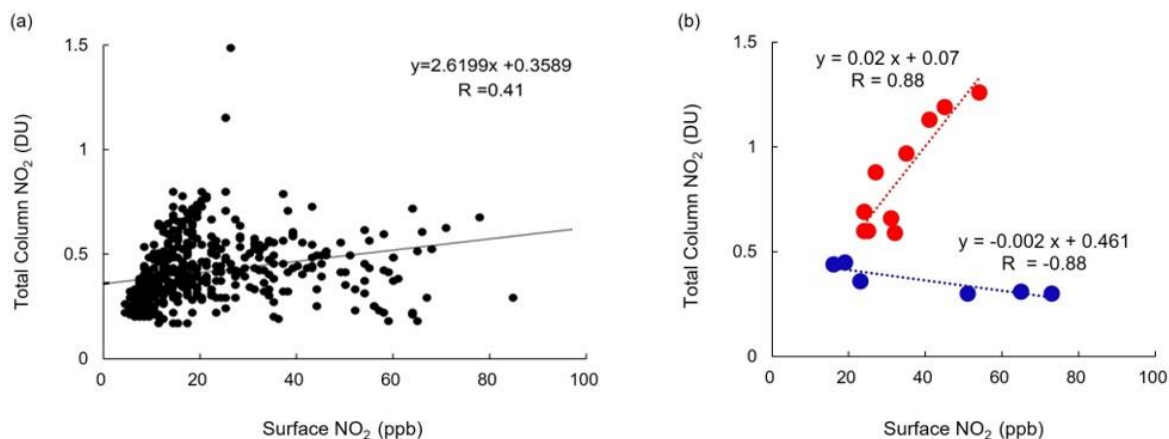
865

866 **Figure 2.** Flight tracks for two Cessna Grand Caravan 208 B aircraft over Pandora sites (left)
 867 PA₄ and (right) PA₁ during the GMAP-2020 campaign. Colored circles indicate airborne NO₂
 868 concentration observations. Stacked circles indicate spiral flights conducted over two sites.

869

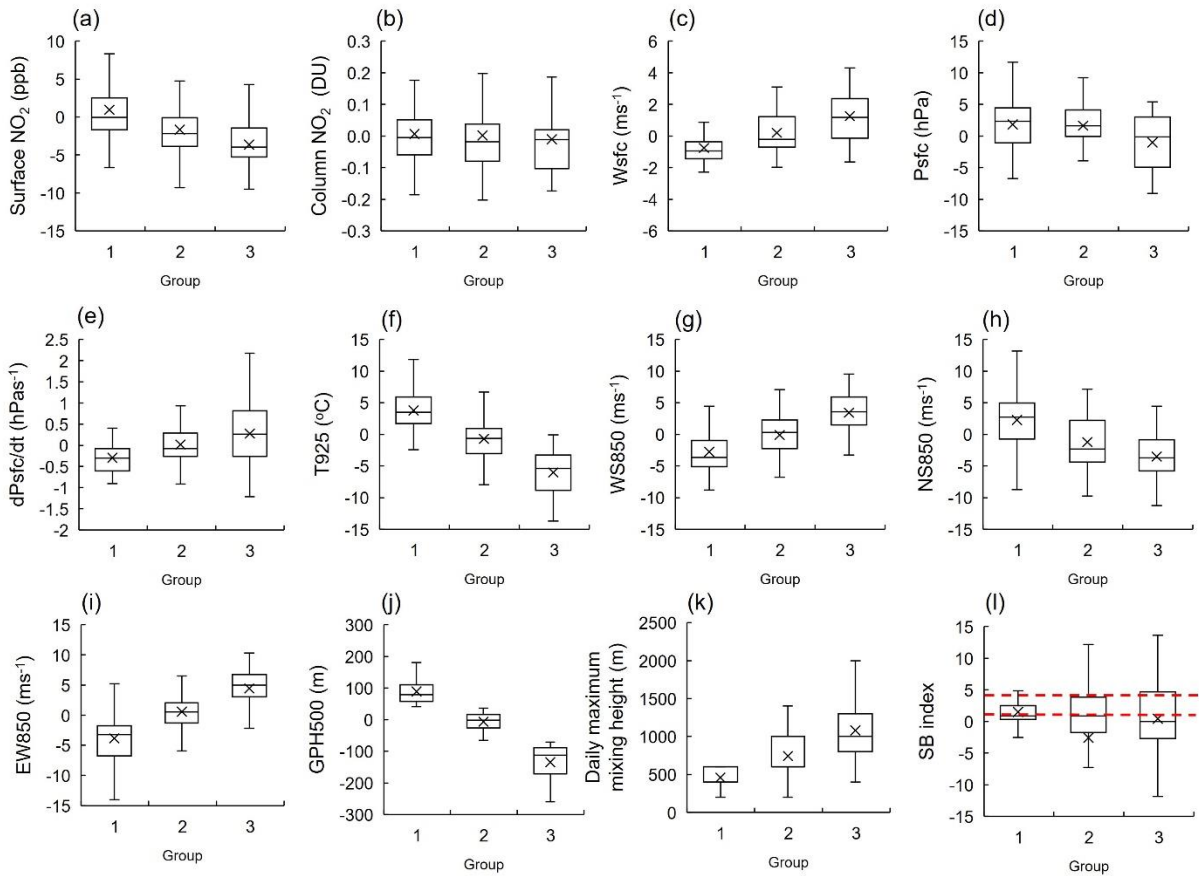
870

871



872

873 **Figure 3.** a) Pandora column (PC) NO₂ measurements as a function of surface *in situ* (SI) NO₂
 874 observations at Pandora sites PA₁–PA₃ during the GMAP-2020 campaign and PA₄ during a 1-
 875 year period. A 1:1 linear regression model was used to evaluate the relationship between PC
 876 and SI measurements (black line). (b) Sample scatterplots of PC-NO₂ and SI-NO₂ for February
 877 24 (red) and April 21 (blue), 2021.



879 **Figure 4.** K-means clustering yielded three groups of cases for (a) surface NO₂ and (b) PC-
 880 NO₂, associated with eight meteorological variables: (c) surface wind speed (Wsfc), (d) Psfc,
 881 (e) Psfc tendency (dPsfc/dt), (f) 925-hPa air temperature (T925), (g) 850-hPa wind speed
 882 (W850), (h) 850-hPa north–south wind component (NS850), (i) 850-hPa east–west wind
 883 component (EW850), and (j) 500-hPa geopotential height (GPH500). All data were de-
 884 seasonalized using the 30-day moving average, except PC-NO₂, for which the monthly average
 885 was used. (k) Simulated daily maximum mixing height (not directly clustered). (l) Box and
 886 whisker plots of the sea breeze index (SBI) at Seosan for the 1-year period. Red dots indicate
 887 the critical SBI (a value of 3), suggested by Biggs and Graves (1962).

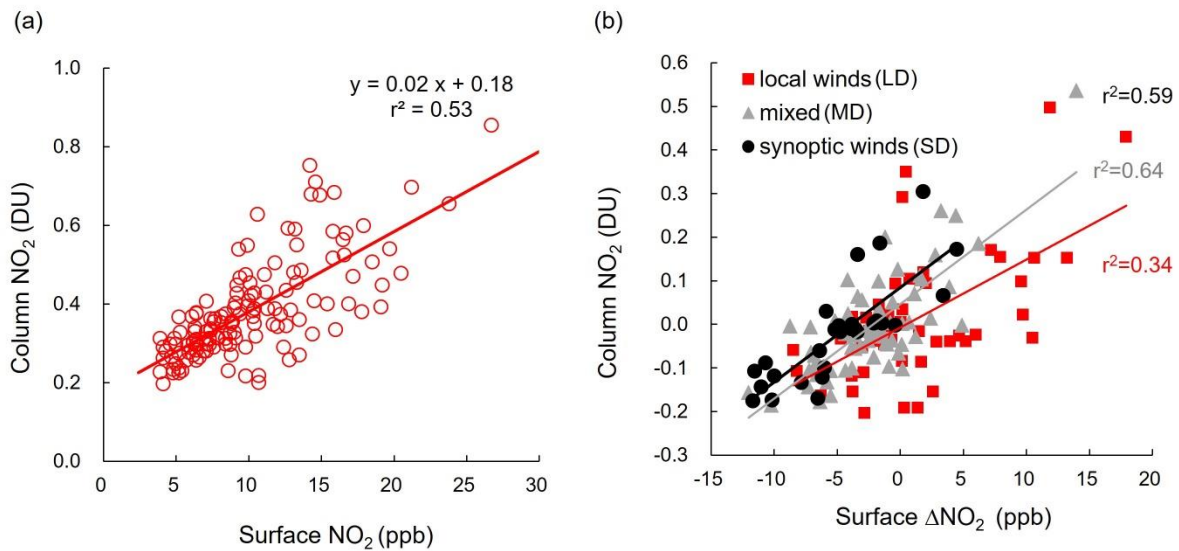
888

889

890

891

892



893

894 **Figure 5.** (a) Scatterplots of daytime measurements at site PA₄ (a) PC-NO₂ vs. SI-NO₂ under
 895 all meteorological conditions and (b) PC-NO₂ vs. Surface Δ NO₂ in each meteorological
 896 condition over a 1-year period (November 12, 2020–October 30, 2021). Here Surface Δ NO₂
 897 = SI-NO₂ – (30-day moving average) SI-NO₂.

898

899

900

901

902

903

904

905

906

907

908

909

910

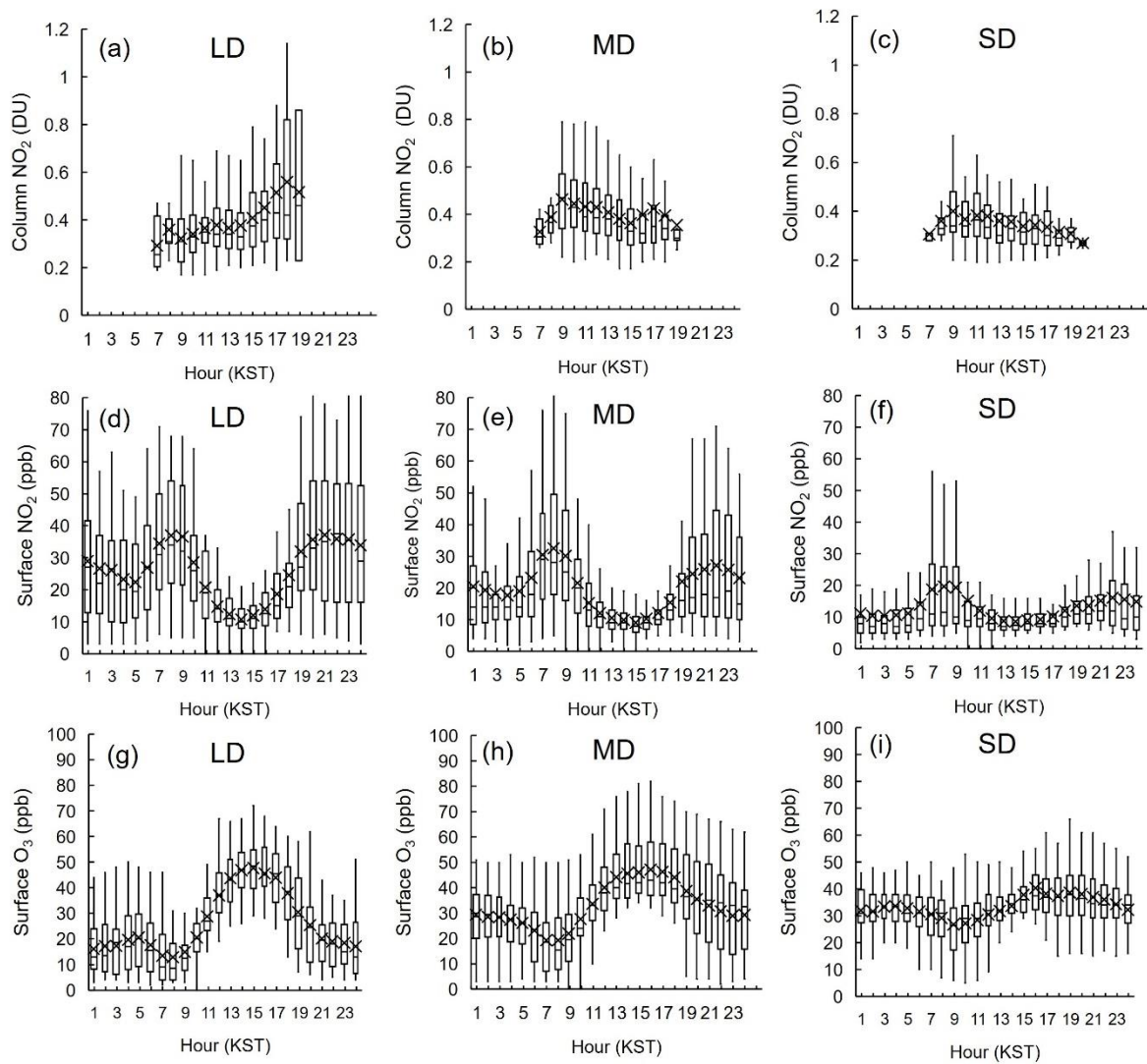
911

912

913

914

915



916

917 **Figure 6.** Box and whisker plots of diurnal variation in (a–c) PC-NO₂, (d–f) SI-NO₂, and (g–
 918 i) surface O₃ under synoptic wind-dominant (SD), mixed (MD), and local wind-dominant (LD)
 919 conditions in Seosan during a 1-year period (November 12, 2020–October 30, 2021).

920

921

922

923

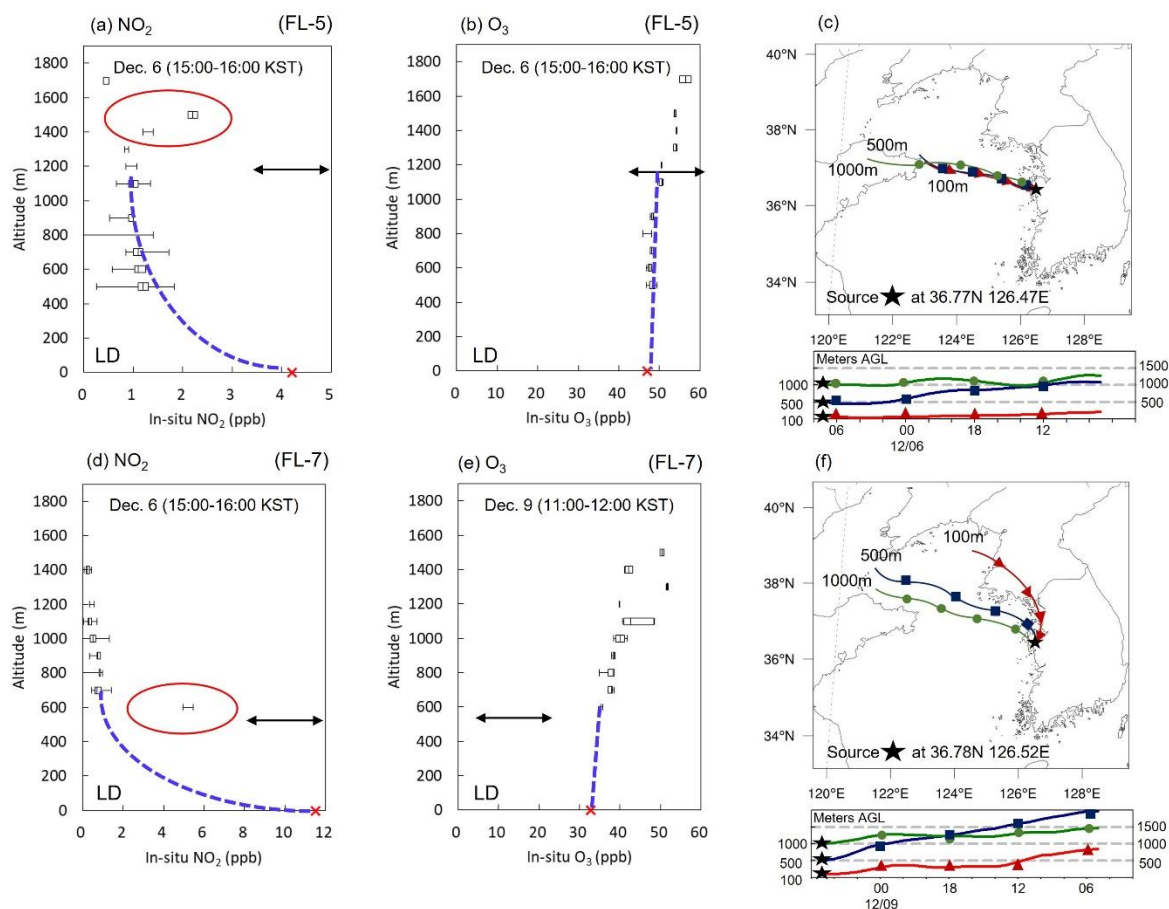
924

925

926

927

928



929

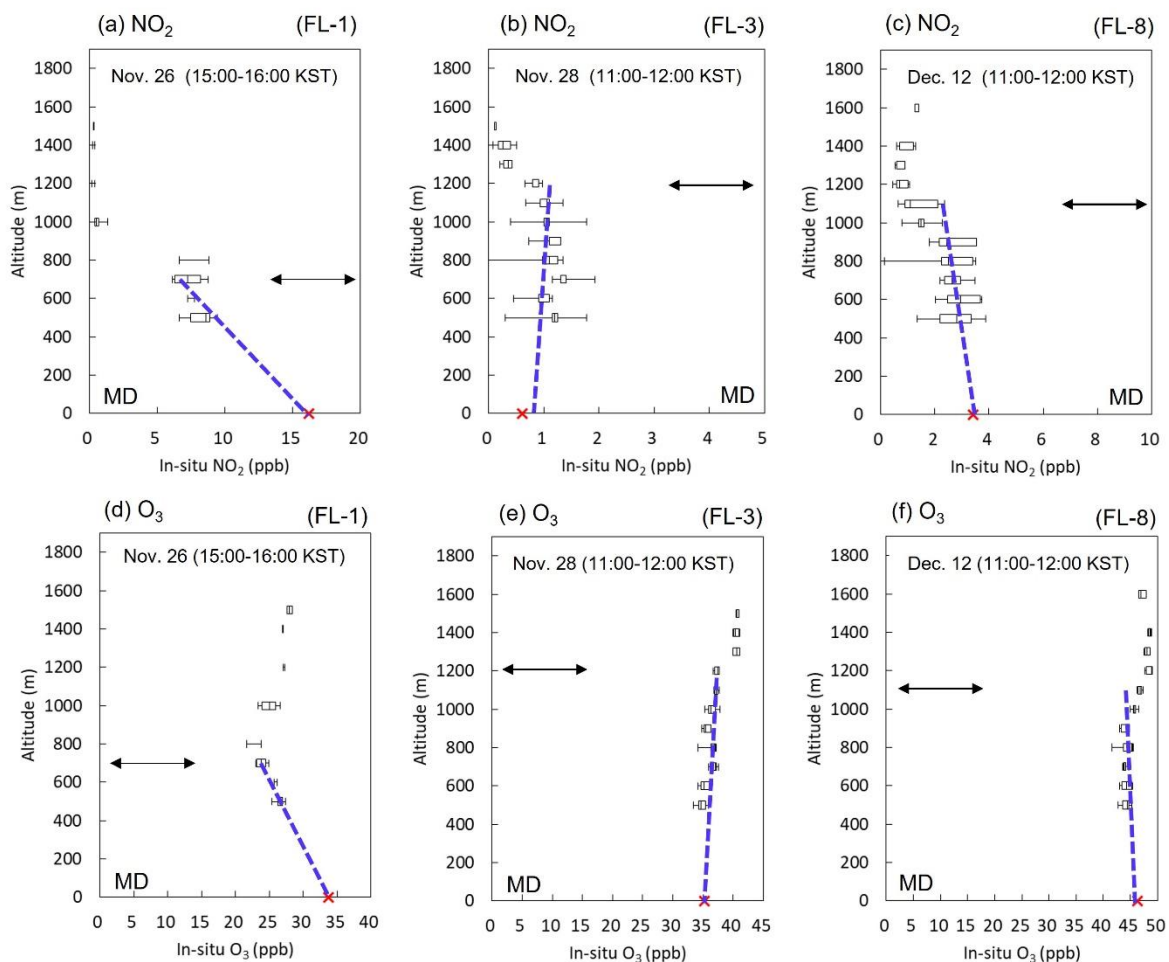
930 **Figure 7.** Box and whisker plots of the vertical NO₂ and O₃ profiles measured by GMAP
931 aircraft superposed with *in situ* AQMS₁ measurements during flights (a, b) FL-5 (December 6)
932 and (d, e) FL-7 (December 6 and 9). Blue dashed lines are linear regression lines fitted to NO₂
933 and O₃ profiles within the planetary boundary layer (PBL). Black arrows indicate the simulated
934 PBL height (PBLH) obtained from the Korea Meteorological Administration (KMA).
935 HSYPLIT 24-h backward trajectories in Seosan are shown at altitudes of 100, 500, and 1,000
936 m, starting at 1600 KST on November 26 and 1200 KST on December 12.

937

938

939

940



942

943 **Figure 8.** Box and whisker plots of vertical profiles obtained from GMAP aircraft superposed
 944 with *in situ* AQMS measurements for (1) NO₂ and (2) O₃ for flights (a) FL-1 (November 26),
 945 (b) FL-3 (November 28), and (c) FL-8 (December 12). Blue dashed lines are linear regression
 946 lines fitted to NO₂ and O₃ in the PBL. Black arrows indicate PBLH simulated by the Hybrid
 947 Single-Particle Lagrangian Integrated Trajectory (HYSPLIT) Global Forecast System (GFS).

948

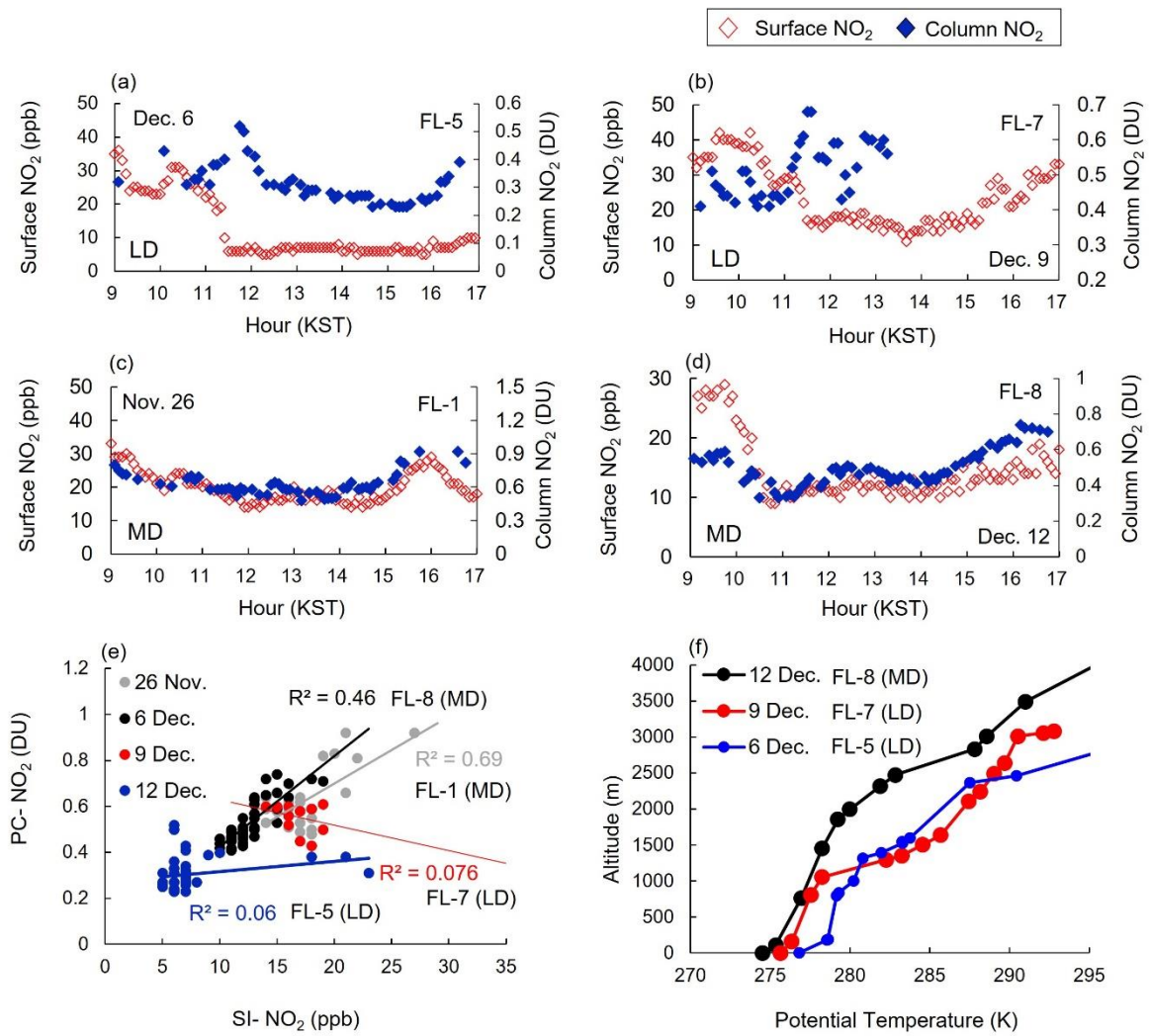
949

950

951

952

953



954

955 **Figure 9.** Time series and scatterplots of PC-NO₂ and SI-NO₂ at PA₂ on (a) December 6, (b)

956 December 9, (c) November 26, and (d) December 12. (e) Scatterplot of PC-NO₂ and SI-NO₂

957 on December 6 (blue), December 9 (red), November 26 (gray), and December 12 (black). (f)

958 Vertical potential temperature profiles on December 6, 9, and 12, 2020. Radiosonde data for

959 November 26, 2020 are missing.

960

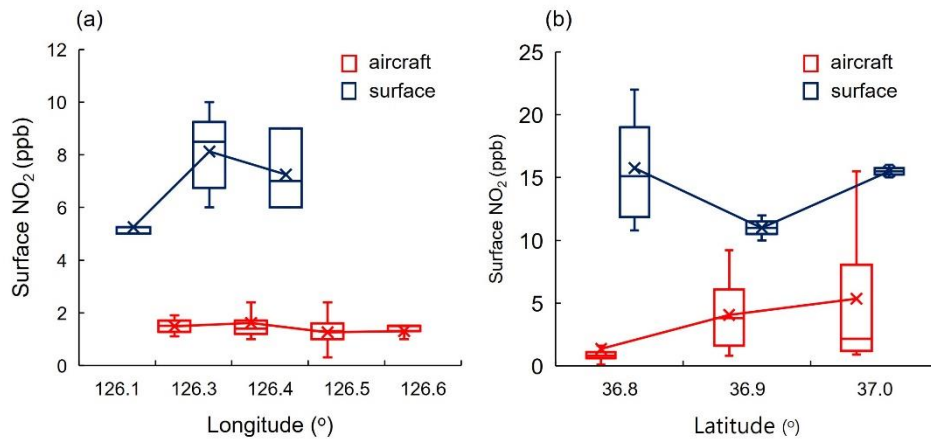
961

962

963

964

965



966

967 **Figure 10.** Latitudinal NO₂ distribution at the surface and 600 m over PA₄ (Seosan Super Site),
 968 averaged during (a) 1300–1600 KST on December 6 (FL-5) by longitude and (b) 1200–1400
 969 KST on December 9 (FL-7) by latitude, obtained from airborne (blue) and surface
 970 measurements (red).

971

972

973

974

975

976

977

978

979

980

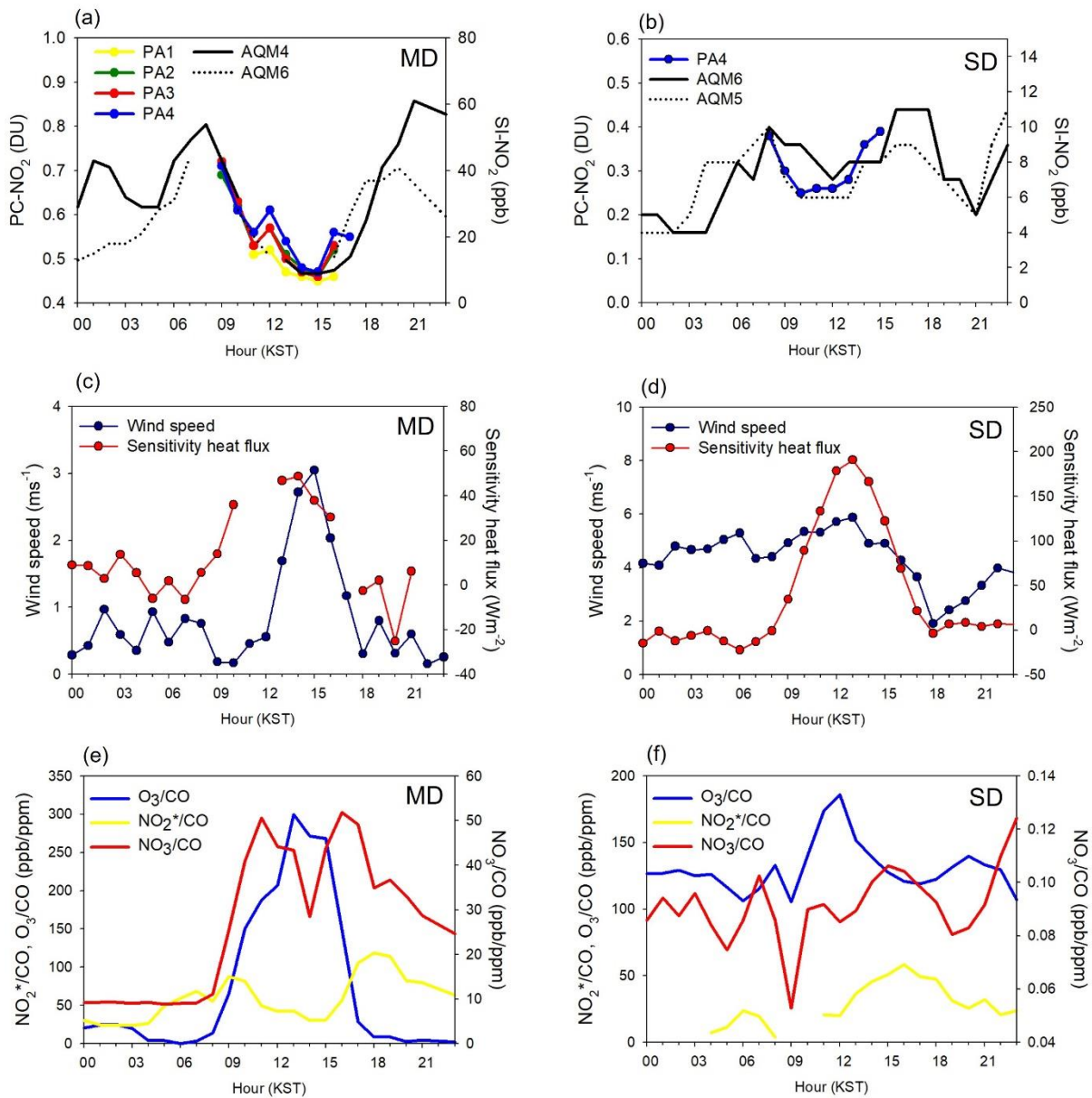
981

982

983

984

985



987

988 **Figure 11.** Examples of the diurnal variation on November 25 (a, c, e) and December 14 (b, d,
 989 f). (a, b) Column NO₂ at sites PA₁–PA₄ and surface NO₂ at air quality monitoring sites AQM₄
 990 and AQM₆. (c, d) Sensible heat fluxes and surface wind speed at PA₄. (e, f) Diurnal variation
 991 in NO₂, NO₂⁺, and O₃ normalized by CO. Figure 1 shows the locations of the measurement
 992 sites.

993

994